

Supplementary Materials for

Optimized Carrier Extraction at Interfaces for 23.6% Efficient Tin–Lead Perovskite Solar Cells

Shuaifeng Hu,¹ Kento Otsuka,¹ Richard Murdey,¹ Tomoya Nakamura,¹ Minh Anh Truong,¹
Takumi Yamada,¹ Taketo Handa,¹ Kazuhiro Matsuda,² Kyohei Nakano,³ Atsushi Sato,⁴
Kazuhiro Marumoto,⁴ Keisuke Tajima,³ Yoshihiko Kanemitsu,¹ Atsushi Wakamiya*¹

*Corresponding author. Email: wakamiya@scl.kyoto-u.ac.jp

This PDF file includes:

Experimental Section
Figs. S1 to S52
Tables S1 to S6
References (1 to 10)

Experimental Section

Materials

Unless otherwise stated, all materials were used as received without further purification. Methylammonium iodide (MAI, >99.0%), formamidinium iodide (FAI, >98.0%), bathocuproine (BCP), lead(II) iodide (PbI₂, 99.99%, trace metals basis), and cesium iodide (CsI, >99%) were purchased from Tokyo Chemical Industry Co., Ltd. (TCI). Ammonium thiocyanate (NH₄SCN, 99.99% trace metals basis), tin(II) fluoride (SnF₂, 99%), and tin(II) iodide (SnI₂, beads, 99.99%, trace metals basis), ethane-1,2-diammonium iodide (ethylenediammonium diiodide, EDAI₂, ≥98%), glycine hydrochloride (GlyHCl, ≥99%), poly[bis(4-phenyl)(2,4,6-trimethylphenyl)amine] (PTAA), and poly(methyl methacrylate) (PMMA) were purchased from Sigma-Aldrich Co., Ltd. (Sigma-Aldrich). Poly(3,4-ethylenedioxythiophene): poly(styrene sulfonate) (PEDOT:PSS) aqueous solution (Clevious PVP AI 4083) was purchased from Heraeus Co., Ltd. Fullerene C₆₀ (sublimed, 99.99%) was purchased from ATR Company. 2,3,5,6-Tetrafluoro-7,7,8,8-tetracyanoquinodimethane (F4-TCNQ) and poly[9,9-dioctyl-9',9'-bis[3-(trimethylammonio)propyl] [2,2'-bi-9H-fluorene]-7,7'-diyl iodide (PFN-I) were purchased from Ossila. Dehydrated dimethylsulfoxide (DMSO, super dehydrated) and isopropanol (IPA, super dehydrated) were purchased from FUJIFILM Wako Pure Chemical Co., Ltd. Dimethylformamide (DMF), toluene and chlorobenzene were purchased from Kanto Chemical. Co., Inc. All of these solvents were degassed by Ar gas bubbling for 1 h and further dried with molecular sieves (3 Å) in an Ar-filled glove box (H₂O, O₂ <0.1 ppm) before use.

Fabrication of Perovskite Thin Films

The perovskite film preparation was conducted in an Ar-filled glove box (H₂O, O₂ <0.1 ppm). The Cs_{0.1}FA_{0.6}MA_{0.3}Sn_{0.5}Pb_{0.5}I₃ perovskite precursor solution was prepared by mixing CsI (46.8 mg, 0.180 mmol), FAI (185.7 mg, 1.08 mmol), MAI (85.8 mg, 0.540 mmol), SnI₂ (335.3 mg, 0.900 mmol), PbI₂ (414.9 mg, 0.900 mmol), SnF₂ (14.1 mg, 0.090 mmol), and NH₄SCN (2.7 mg, 0.036 mmol) in mixed solvents of 0.25 mL DMSO and 0.75 mL DMF to reach a concentration of 1.8 M. To prepare the samples with additive, 2 mol% (4.0 mg, 0.036 mmol) of GlyHCl with respect to the total amount of SnI₂ and PbI₂ was added to the precursor solution. The precursor solution was stirred at 45 °C for 40 min and filtered through a 0.20 μm PTFE filter before use. To spin coat the

films, 200 μL of the room temperature precursor solution was applied to the substrate. A two-step spin coating program was used. The first step was at 1000 rpm for 10 s with an acceleration of 200 rpm s^{-1} , and the second step was 4000 rpm for 40 s with an acceleration of 1000 rpm s^{-1} . Room temperature chlorobenzene (400 μL) was used as the antisolvent. The chlorobenzene was quickly dripped onto the surface of the spinning substrate over an interval of 1 s during the second spin coating step at 20 s before the end of the procedure. The substrate was then immediately annealed on a 100 $^{\circ}\text{C}$ hot plate for 10 min, followed by annealing at 65 $^{\circ}\text{C}$ for over 10 min. For the EDAI_2 post-treatment, 1.0 mg EDAI_2 was added to 1.0 mL IPA and 1.0 mL toluene. The mixed solvent solution was stirred at 70 $^{\circ}\text{C}$ for 3 h and then filtered through a 0.20 μm PTFE filter before spin coating. 120 μL of the EDAI_2 solution was applied to the annealed and cooled perovskite films by spin coating at 4000 rpm for 20 s with an acceleration of 1333 rpm s^{-1} . Following spin coating, the films were immediately annealed again at 100 $^{\circ}\text{C}$ for around 5 min (see more detail at Fig. S47).

For the space-charge-limited current (SCLC) measurements, hole-only and electron-only devices were prepared. For the hole-only devices, 150 μL PTAA solution (20 mg mL^{-1} in chlorobenzene, doped with 1 wt% F4-TCNQ) was spin-coated onto the perovskite films fabricated on the PEDOT:PSS-coated substrates at 2000 rpm for 30 s with an acceleration of 400 rpm s^{-1} , and the films were immediately annealed at 65 $^{\circ}\text{C}$ for around 5 min. For the electron-only devices, double-sided C_{60} layers (20 nm) were sequentially deposited by thermal evaporation before and after the perovskite layer preparation. For all samples, 100 nm of silver was deposited through a metallic aperture mask to form the top electrode.

For the films fabricated on PTAA/PFN-coated FTO, 120 μL PTAA solution (2 mg mL^{-1} in chlorobenzene) was spin-coated onto the FTO substrates at 4000 rpm for 20 s, and the films were immediately annealed at 130 $^{\circ}\text{C}$ for around 10 min. Then, the PTAA-coated FTO substrates were coated with PFN-I. 120 μL PFN-I solution (0.1 mg mL^{-1} in DMF) was spin-coated onto the PTAA-coated FTO substrates at 4000 rpm for 20 s without annealing.

Fabrication of solar cell devices

Glass/FTO substrates (10 $\Omega \text{ sq}^{-1}$, AGC Inc.) were etched with zinc powder and HCl (6 M in deionized water), and consecutively cleaned with 15 min ultrasonic bath in water, acetone, detergent

solution (Semico Clean 56, Furuuchi chemical), water, and isopropanol, followed by drying with an air gun, and finally plasma treatment. The PEDOT:PSS hole transport layer was fabricated from an aqueous dispersion which was filtered through a 0.45 μm PVDF filter and then spin coated on the FTO substrate using a spin program of 10 s at 500 rpm followed by 30 s at 4000 rpm. The films were then annealed in air at 140 $^{\circ}\text{C}$ for 20 min. After transferring to an Ar-filled glove box (H_2O , $\text{O}_2 < 0.1$ ppm), the substrates were degassed at 140 $^{\circ}\text{C}$ for 30 min. The perovskite layer was fabricated on PEDOT:PSS following the above-mentioned procedure. The samples were moved under Ar to a vacuum deposition chamber, where 20 nm of C_{60} (deposition rate 0.01 nm s^{-1}) and 8 nm of BCP (deposition rate 0.01 nm s^{-1}) were deposited by thermal evaporation. The top electrode was prepared by depositing 100 nm of silver (Ag) through a shadow mask. The deposition rate for Ag was firstly set as 0.005 nm s^{-1} to reach 5 nm, then raised to 0.01 nm s^{-1} to reach 20 nm, and finally raised to 0.08 nm s^{-1} to reach the target thickness.

Characterization

For the time-resolved photoluminescence (TRPL) measurements, the samples were excited by a picosecond pulsed laser with a wavelength of 688 nm (Advanced Laser Diode System) and the excitation frequency of 10 kHz. To shorten the measurement time, the PL signal was divided with a beam splitter (transmission 50%) and detected with a pair of avalanche photodiodes (APD) (ID Quantique). The TRPL signal on each APD was recorded using time-correlated single photon counting boards (Pico Quant). Under weak excitation conditions, a defocus lens was used in order to maintain a high incident photon flux into the APDs. The initial carrier densities were calculated from the excitation photon flux and the absorption coefficient of samples at 688 nm ($4.4 \times 10^4 \text{ cm}^{-1}$, Fig. S29). Using a variable neutral density filter, the excitation laser power was adjusted to achieve the desired initial carrier density. The TRPL dynamics were analyzed by the rate equation model reported in our previous work¹.

Scanning electron microscopy (SEM) was performed with a Hitachi S8010 ultra-high-resolution scanning electron microscope (Hitachi High-Tech Corporation).

UV-vis absorption measurement was performed with a Shimadzu UV-3600 plus spectrometer (Shimadzu Co., Ltd.).

Dynamic light scattering (DLS) was conducted with an ELSZ-2000 spectrophotometer (Otsuka Electronics Co., Ltd., Japan). The experiment was conducted after around five hours before the sample preparation, as the sample transporting to, and equipment adjustment in, the company. The refractive indices and viscosity of the solvent were 1.4405 and 1.1005, respectively, based on the DMF and DMSO with the volume ratio of 3 to 1.

X-ray photoelectron spectroscopy (XPS) was recorded with a JPS-9010 (JEOL Co., Ltd.) instrument. Perovskite film samples for XPS measurements were prepared in an Ar-filled glove box and transferred to the XPS chamber through an Ar-filled transfer vessel in order to avoid oxygen contamination.

Photocurrent–voltage (J – V) curves were measured in a N₂-filled glove box (H₂O, O₂ <0.1 ppm) with an OTENTO-SUN-P1G solar simulator (Bunkoukeiki Co., Ltd.). The light intensity of the illumination source was calibrated using a standard silicon photodiode. Each device was measured with a 10 mV voltage step and a 100 ms time step (i.e. scan rate of 0.1 V s⁻¹) using a Keithley 2400 source meter. The device active area was defined by an optimal mask, 0.0985 cm² for the regular devices and 1 cm² for the large area cells. Steady-state power output (SPO) measurements were performed by holding the device at the voltage of the maximum power point, as determined by the JV characteristic, and monitoring the current density over the course of 300 s.

External quantum efficiency (EQE) and internal quantum efficiency (IQE) spectra were measured with a Bunkoukeiki SMO-250III system equipped with a Bunkoukeiki SM-250 diffuse reflection unit (Bunkoukeiki Co., Ltd.). The incident light intensity was calibrated with a standard SiPD S1337-1010BQ silicon photodiode.

UPS was performed with a photoelectron spectroscopy system (PHI5000 Versa Probe II, ULVAC-PHI Inc.) with He I excitation (21.22 eV). A –5.0 V bias was applied to the samples. The chamber base pressure was approximately 1 × 10⁻⁶ Pa. Samples were transferred from the glove box to the UPS chamber without exposure to air.

ESR measurements were performed with an X-band ESR spectrometer (JEOL RESONANCE, JES-FA200). The parameters for the measurement are as follow. Sweep range, 319 ± 5 mT; sweep time, 2 min; microwave power, 0.5 mW; modulation frequency, 100 kHz; modulation width, 0.3 mT; time constant, 0.1 s; amplitude, 4000; number of scans (accumulation), 29×10 .

Grazing incidence X-ray diffraction (GIXD) measurements were performed on Rigaku SmartLab equipped with a hybrid pixel array detector HyPix-3000. Perovskite films were deposited on the surface of PEDOT:PSS with glass/FTO as substrates and covered with a thin film of spin-coated poly(methyl methacrylate) (PMMA, Sigma-Aldrich) to prevent direct exposure to air.

^1H NMR spectra were recorded on Bruker Avance-400 spectrometer (400 MHz). The NMR chemical shifts are reported in ppm relative to the residual protons and carbons of DMSO- d_6 ($\delta = 2.50$ ppm in ^1H NMR).

Quantum yields were determined with a Hamamatsu Photonics Quantaurus-QY Plus C13534 with calibrated integrating sphere system.

Electrochemical impedance spectroscopy data were obtained in inert atmosphere under AM1.5G simulated solar radiation, using an Agilent E4990A impedance analyzer. Scans were taken from 20 Hz to 20 MHz, with a 30 mV oscillator voltage, recorded for forward bias voltages between 0 and 1.2 V in 0.1 V steps.

Time-of-flight secondary ion mass spectrometry (ToF-SIMS) measurements were carried out using a ToF.SIMS 5 (IONTOF GmbH) operated in the high lateral resolution mode (burst alignment mode). A 50 kV Bi_3^{2+} primary ion beam with pulses width of 125 ns was used for data acquisition. Primary ion dose density (PIDDD) was maintained less than approximately 5×10^{11} ions cm^{-2} in each measurement cycles to prevent sample damage from the irradiation of primary ion beam. For sample etching, a 10 kV Ar gas cluster ion beam (Ar-GCIB) with a center size of approximately 1200 atoms was used as sputtering ion beam. The raster area of the primary ion beam was $30 \mu\text{m} \times 30 \mu\text{m}$ and that of the sputtering ion beam was 500×500 . Depth profiles and three-dimensional images of EDAl₂/GlyHCl-treated ingredients (or ions) were reconstructed from

the raw data after data acquisition. In addition, mass spectra and depth profiles with high mass resolution were acquired from an area of $200\ \mu\text{m} \times 200\ \mu\text{m}$ by using high mass resolution mode (bunching mode). A low-energy electron-flood gun was used for charge compensation.

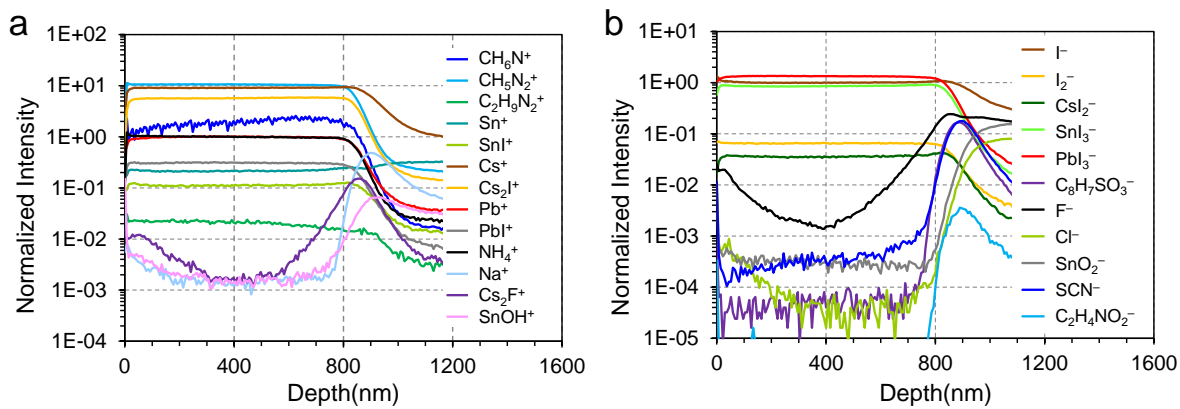


Fig. S1. ToF-SIMS depth profiles of the control perovskite film fabricated on an PEDOT:PSS/FTO-coated glass substrate measured in **a**, positive and **b**, negative polarity.

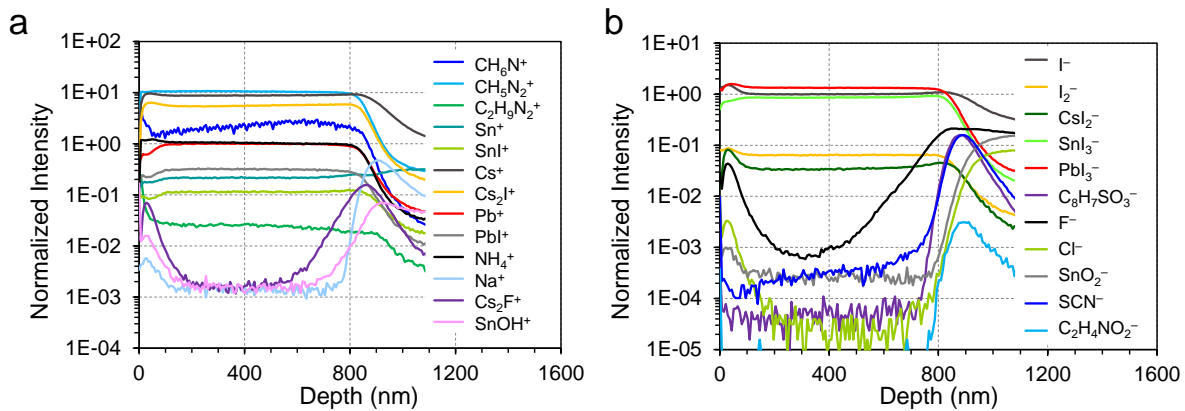


Fig. S2. ToF-SIMS depth profiles of the EDAl₂-treated perovskite film fabricated on an PEDOT:PSS/FTO-coated glass substrate measured in **a**, positive and **b**, negative polarity.

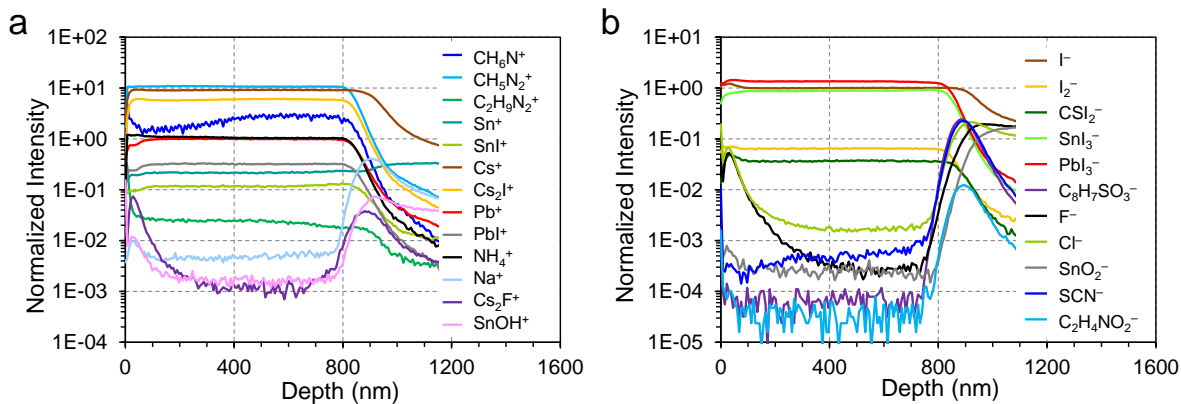


Fig. S3. ToF-SIMS depth profiles of the EDAl₂/GlyHCl-treated perovskite film fabricated on an PEDOT:PSS/FTO-coated glass substrate measured in **a**, positive and **b**, negative polarity.

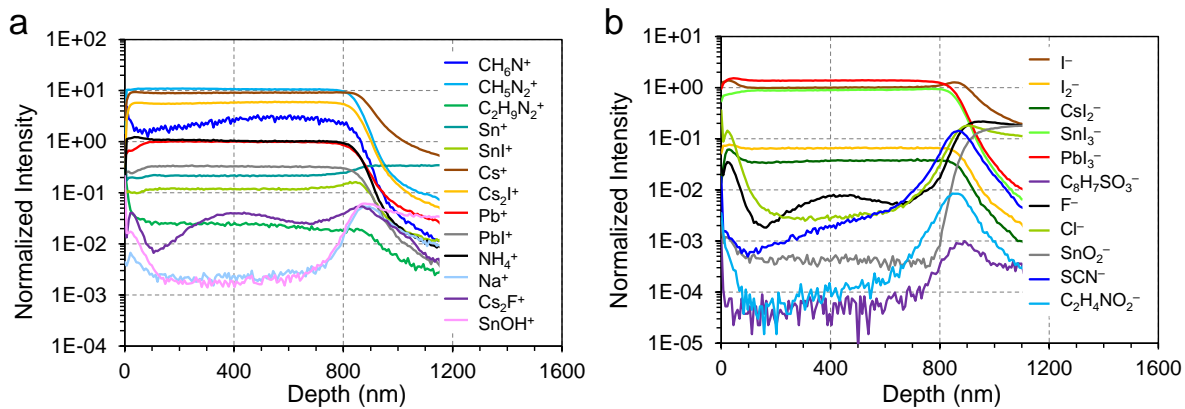


Fig. S4. ToF-SIMS depth profiles of the EDAl₂/GlyHCl-treated perovskite film fabricated on an FTO-coated glass substrate with no PEDOT:PSS layer measured in **a**, positive and **b**, negative polarity.

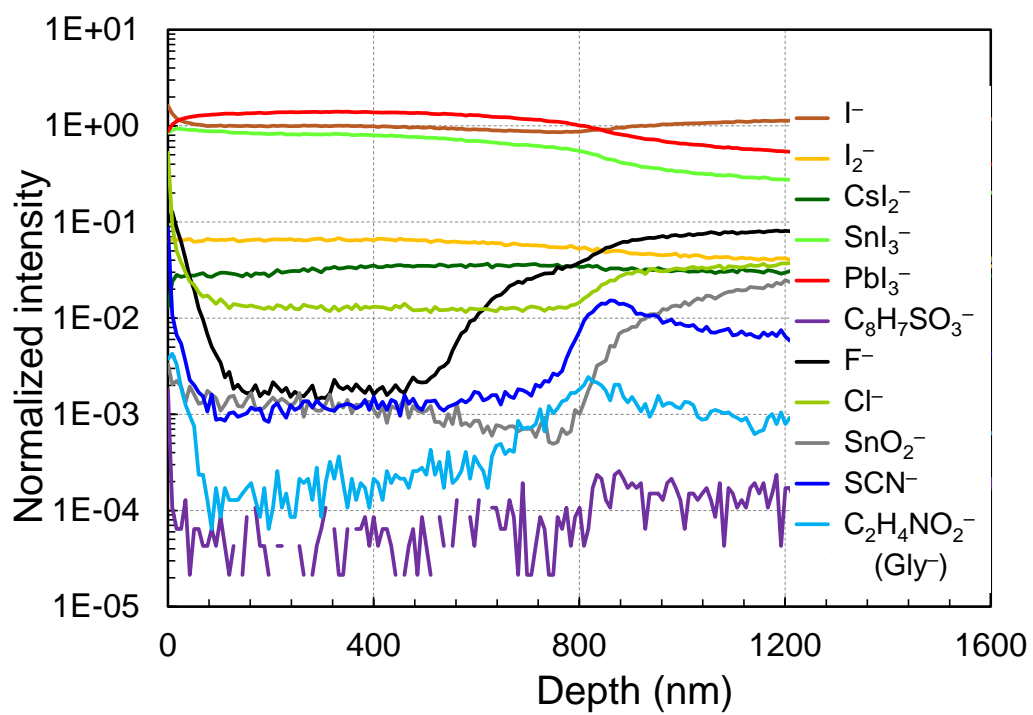


Fig. S5. ToF-SIMS depth profiles of the GlyHCl-treated perovskite films fabricated on PTAA/PFN-coated FTO substrates measured in negative polarity.

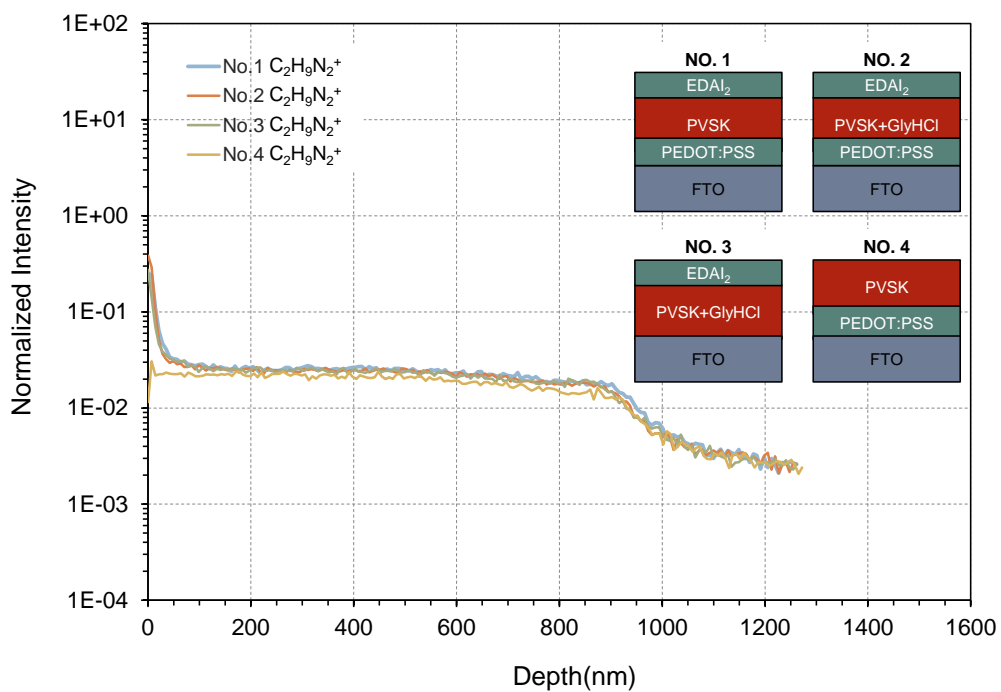


Fig. S6. ToF-SIMS depth profile of EDA²⁺ ions in the different perovskite films: **No. 1**, EDA₂ - treated, **No. 2**, EDA₂/GlyHCl-treated, **No. 3**, EDA₂/GlyHCl-treated without PEDOT:PSS and **No. 4**, Control perovskite films.

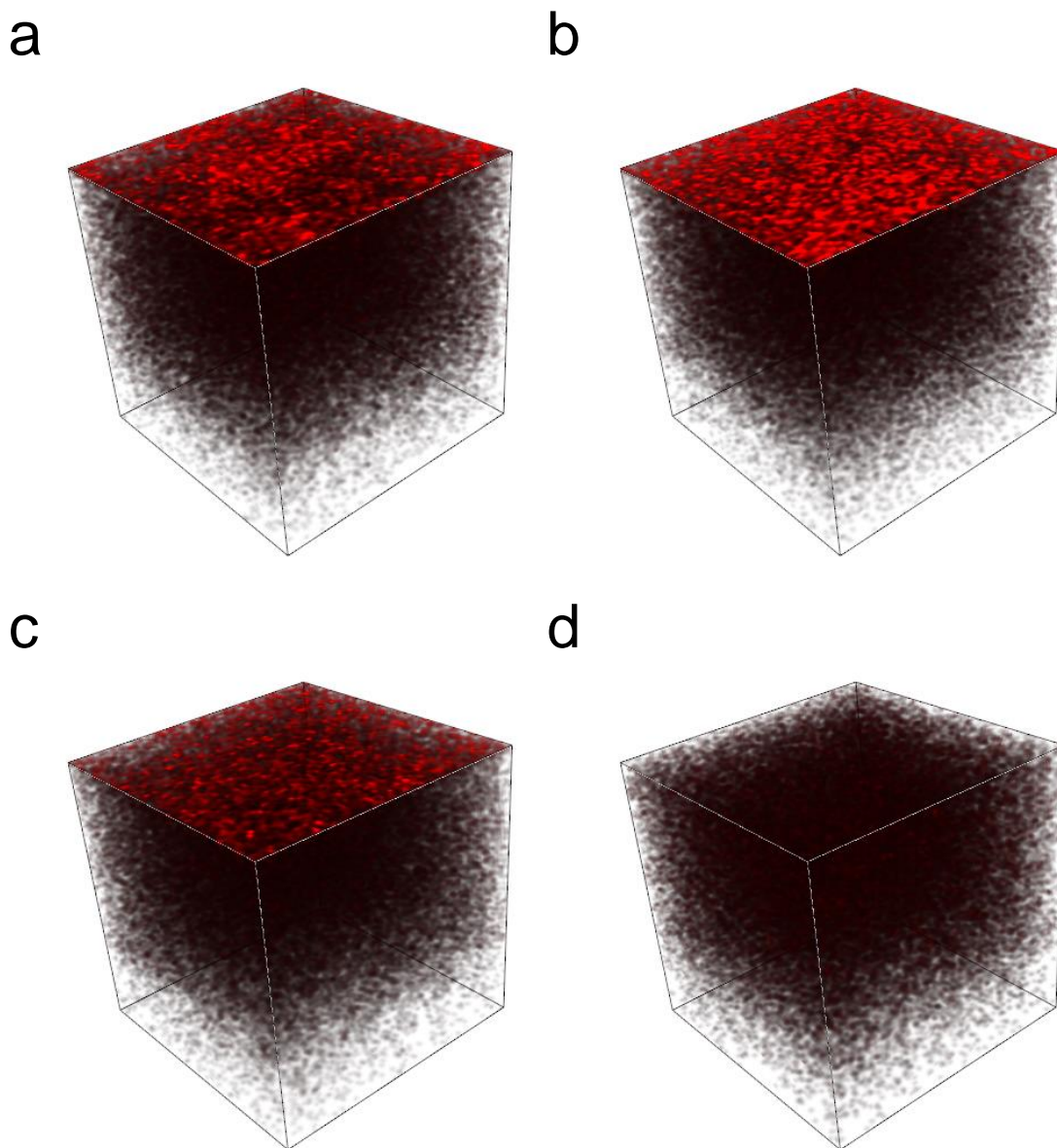


Fig. S7. Reconstructed 3D map (stretched in the z direction for clarity) showing the distributions of EDA²⁺ ions through the perovskite films without subtracting the background signals. **a**, EDAI₂-treated, **b**, EDAI₂/GlyHCl-treated, **c**, EDAI₂/GlyHCl-treated without PEDOT:PSS and **d**, Control perovskite films.

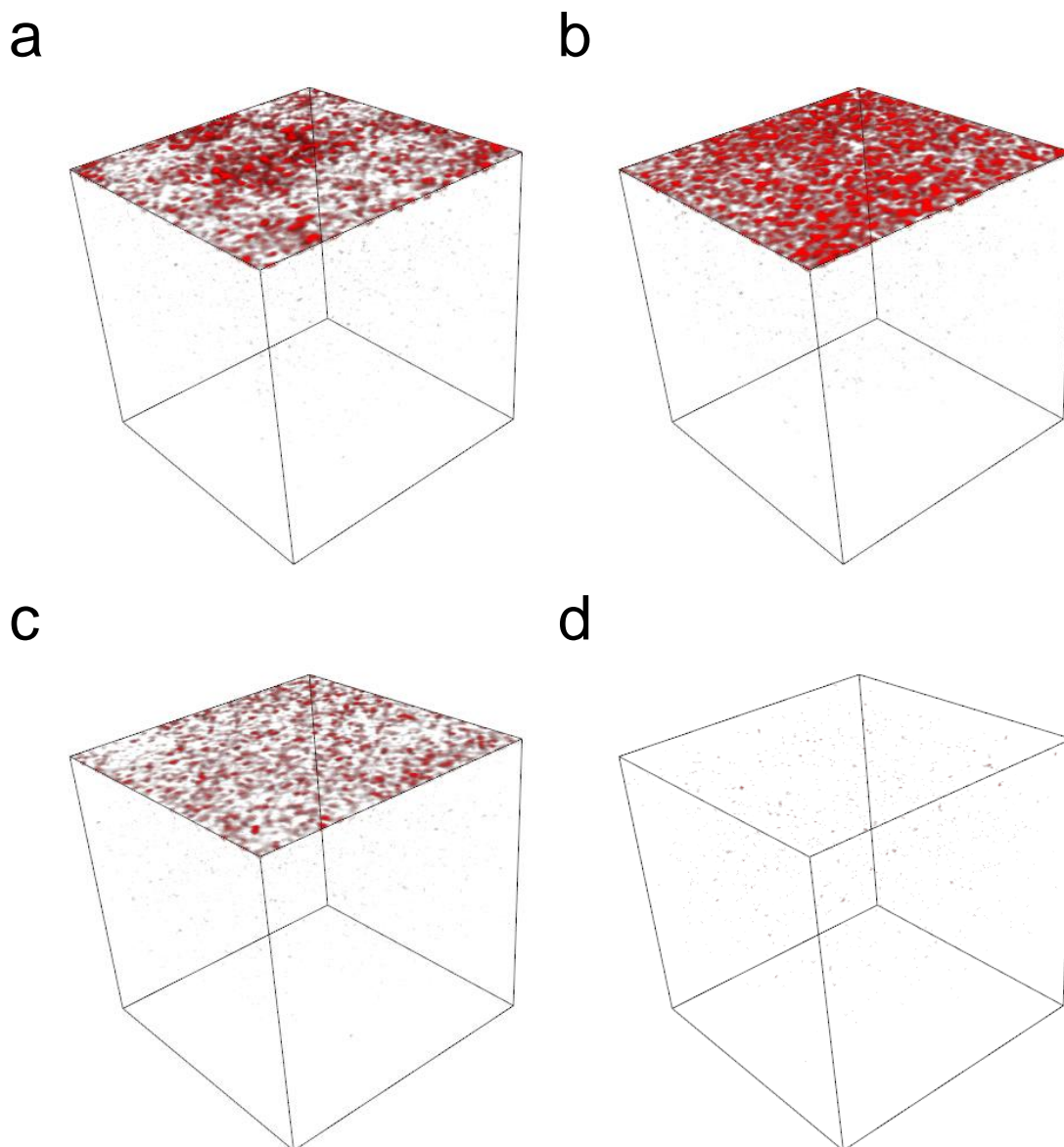


Fig. S8. Reconstructed 3D map (stretched in the z direction for clarity) showing the distributions of EDA²⁺ ions through the perovskite films after subtracting the background signals. **a**, EDAI₂-treated, **b**, EDAI₂/GlyHCl-treated, **c**, EDAI₂/GlyHCl-treated without PEDOT:PSS and **d**, Control perovskite films.

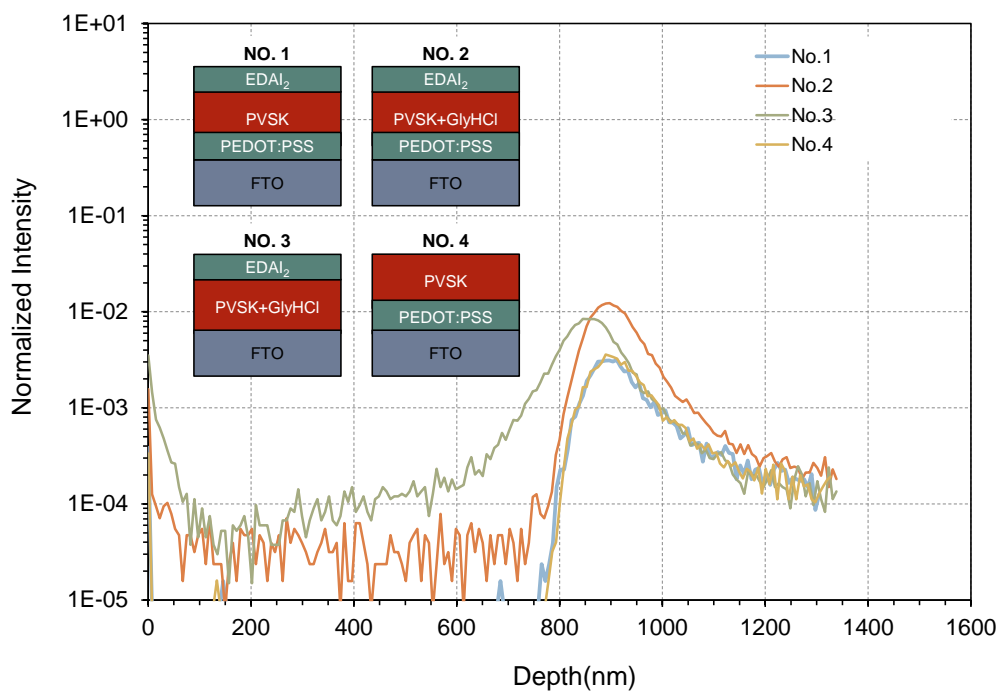


Fig. S9. ToF-SIMS depth profile of GlyH⁺ ions in the perovskite films, inserted figures show the corresponding sample information. **No. 1**, EDAI₂-treated, **No. 2**, EDAI₂/GlyHCl-treated, **No. 3**, EDAI₂/GlyHCl-treated without PEDOT:PSS and **No. 4**, Control perovskite films.

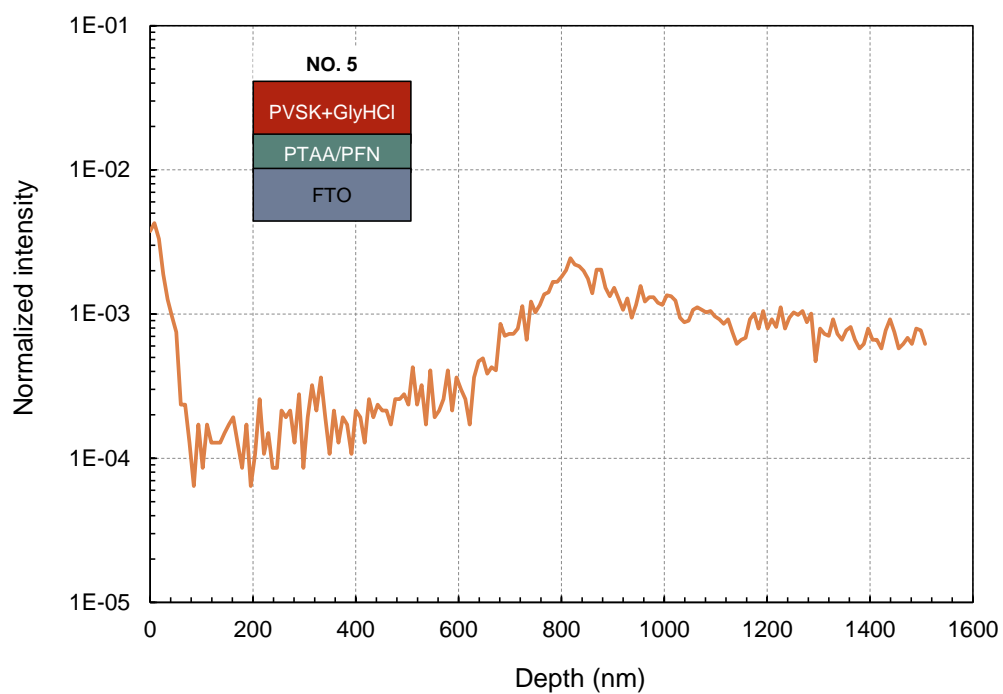


Fig. S10. ToF-SIMS depth profile of GlyH⁺ ions in the perovskite films fabricated on PTAA/PFN-coated FTO substrates.

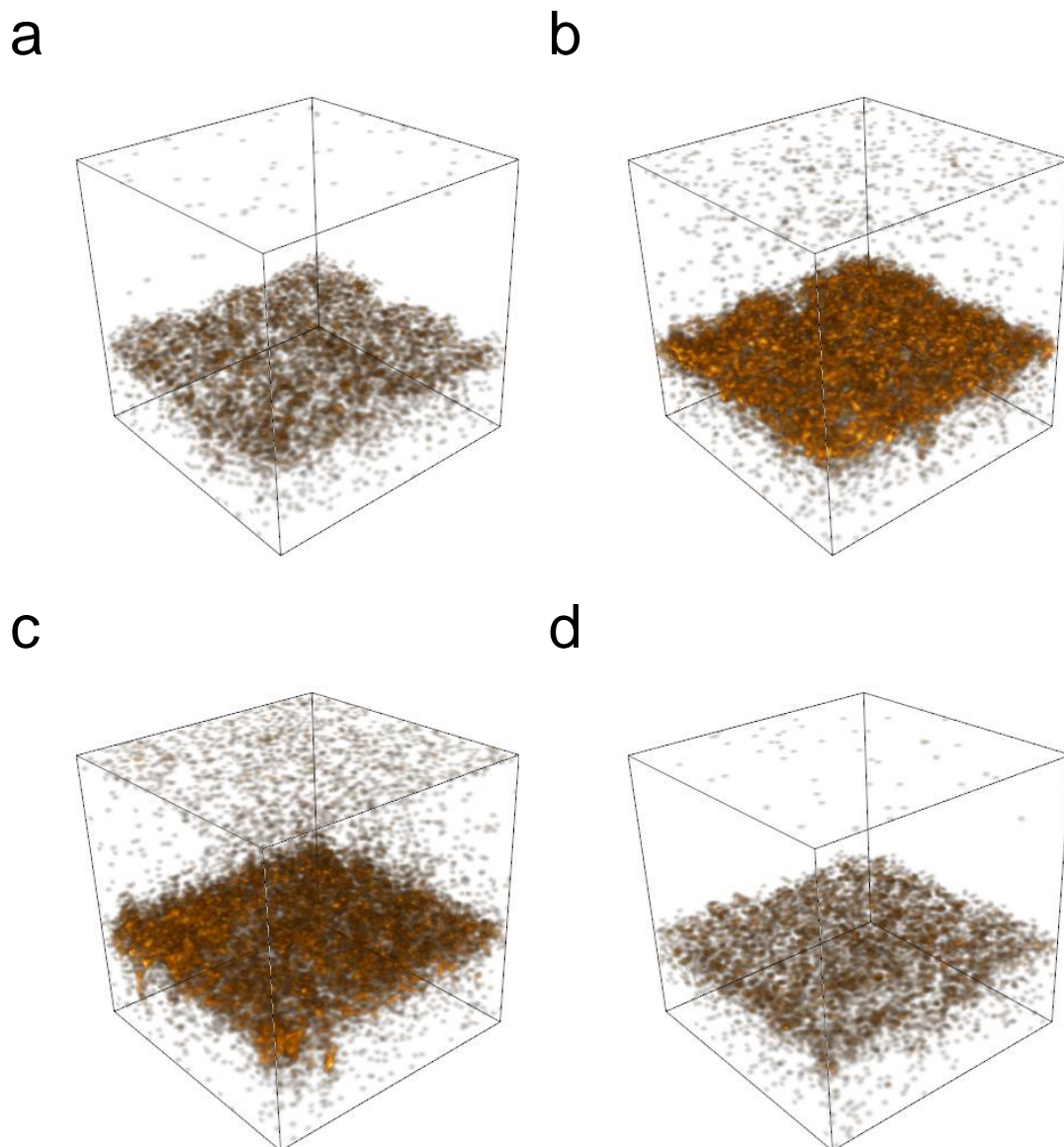


Fig. S11. Reconstructed 3D map (stretched in the z direction for clarity) showing the distributions of GlyH⁺ ions through the perovskite films without subtracting the background signals. **a**, EDAI₂-treated, **b**, EDAI₂/GlyHCl-treated, **c**, EDAI₂/GlyHCl-treated without PEDOT:PSS and **d**, Control perovskite films.

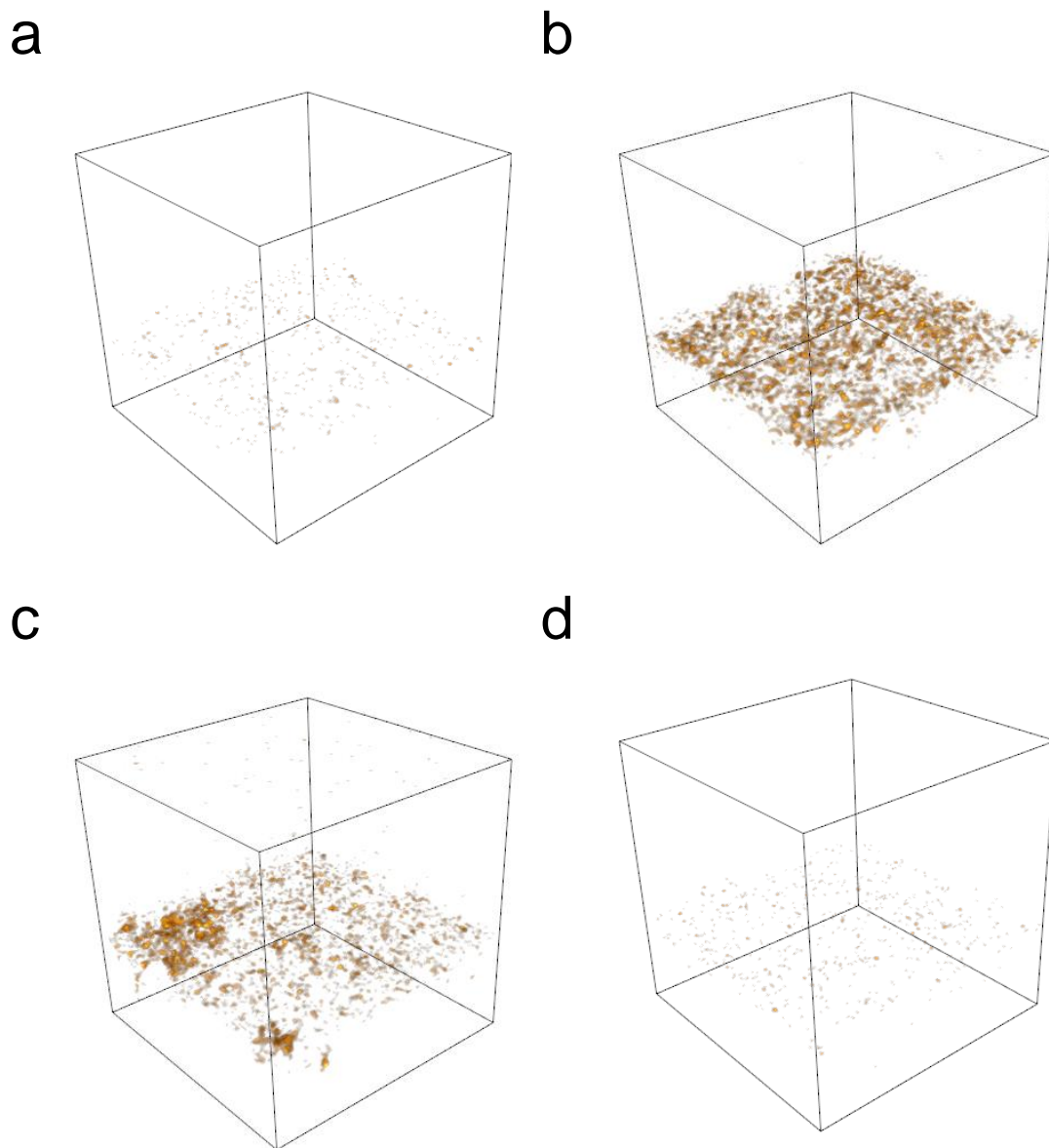


Fig. S12. Reconstructed 3D map (stretched in the z direction for clarity) showing the distributions of GlyH⁺ ions through the perovskite films after subtracting the background signals. **a**, EDAI₂-treated, **b**, EDAI₂/GlyHCl-treated, **c**, EDAI₂/GlyHCl-treated without PEDOT:PSS and **d**, Control perovskite films.

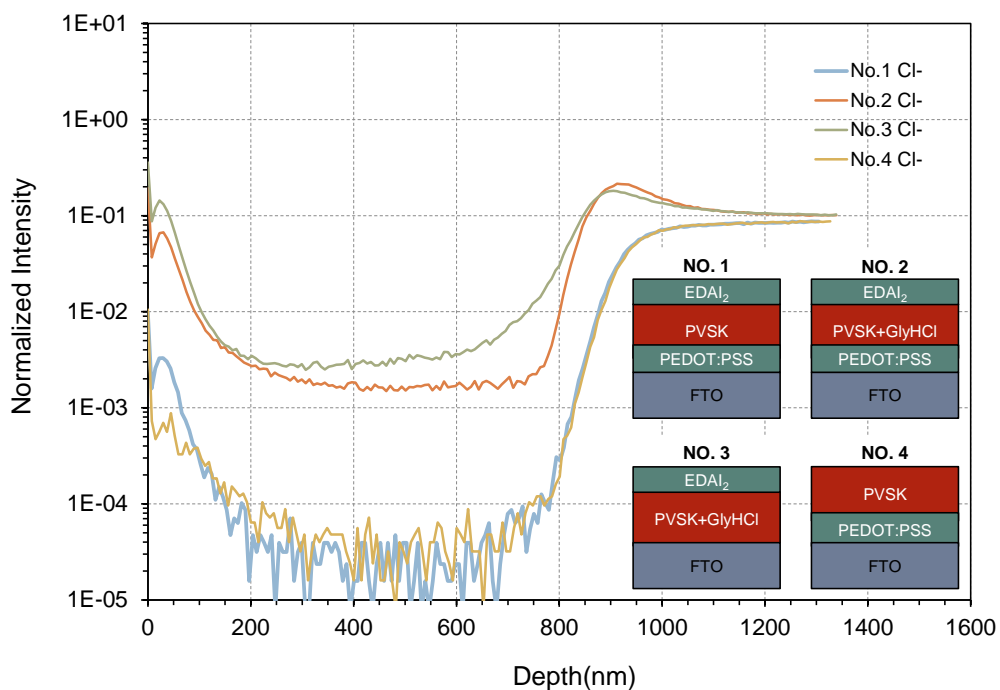


Fig. S13. ToF-SIMS depth profile of Cl⁻ ions in the perovskite films, inserted figures show the corresponding sample information. **No. 1**, EDAI₂-treated, **No. 2**, EDAI₂/GlyHCl-treated, **No. 3**, EDAI₂/GlyHCl-treated without PEDOT:PSS and **No. 4**, Control perovskite films.

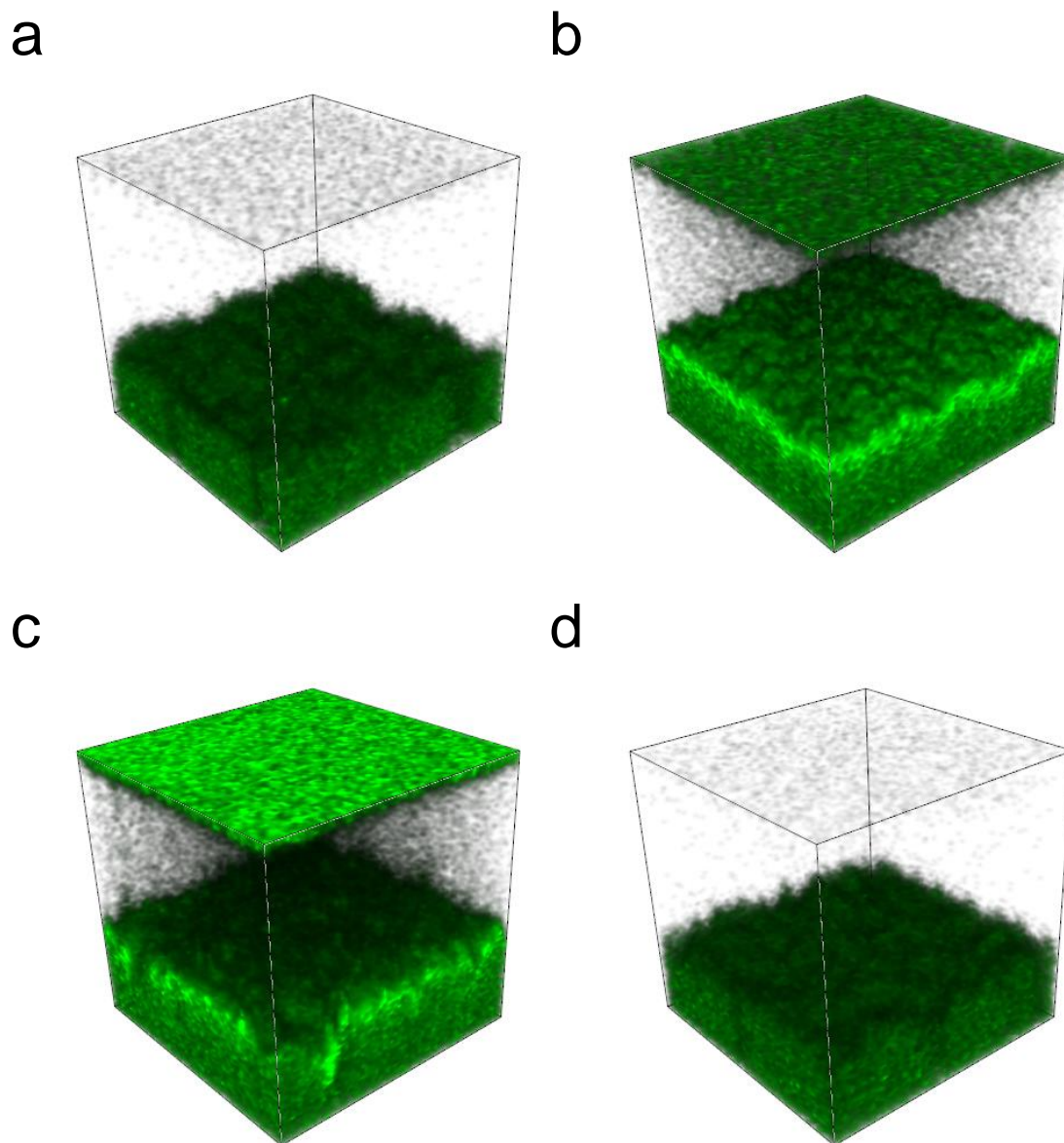


Fig. S14. Reconstructed 3D map (stretched in the z direction for clarity) showing the distributions of Cl⁻ ions through the perovskite films without subtracting the background signals. **a**, EDAI₂-treated, **b**, EDAI₂/GlyHCl-treated, **c**, EDAI₂/GlyHCl-treated without PEDOT:PSS and **d**, Control perovskite films.

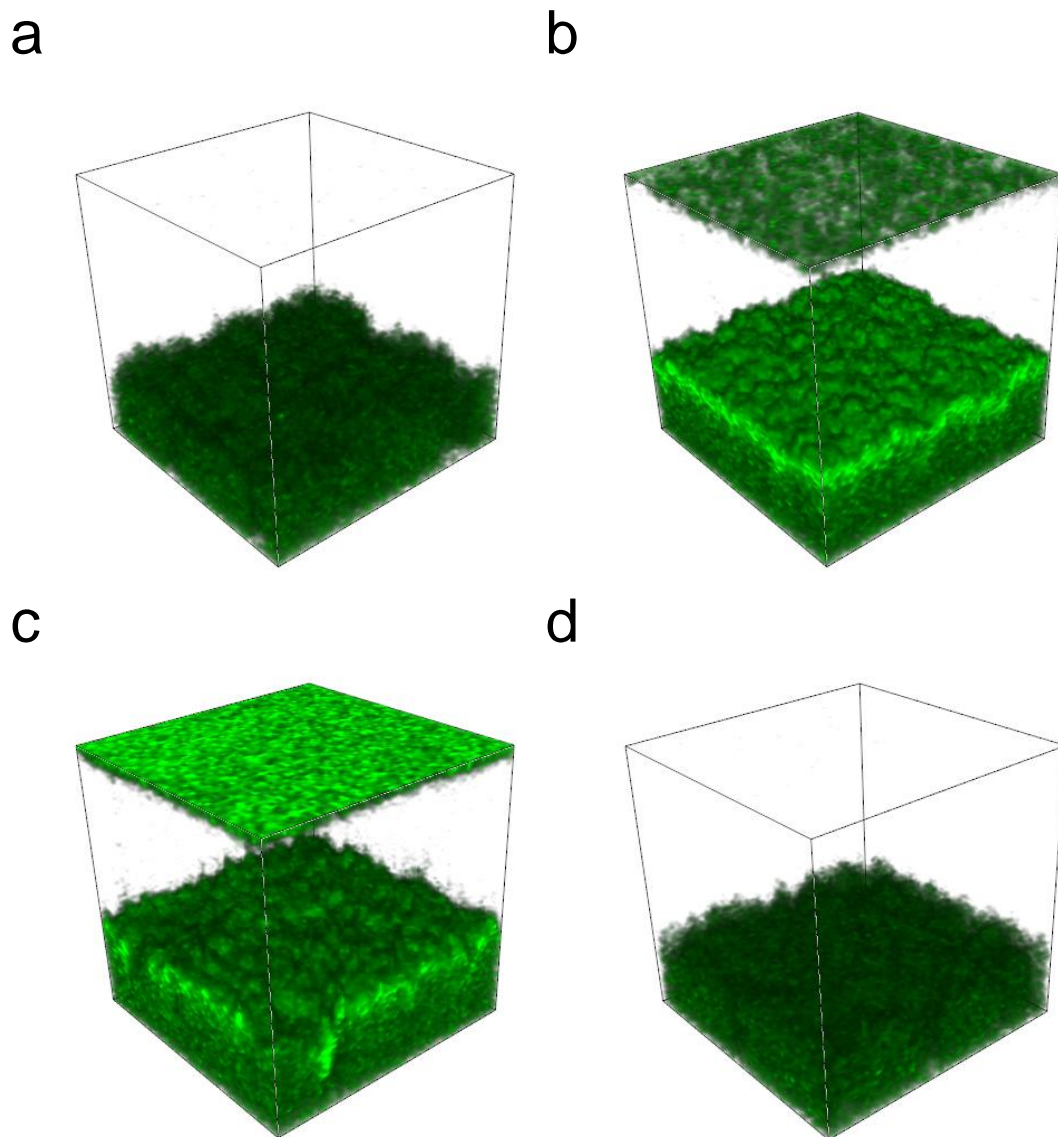


Fig. S15. Reconstructed 3D map (stretched in the z direction for clarity) showing the distributions of Cl^- ions through the perovskite films after subtracting the background signals. **a**, EDAI_2 -treated, **b**, $\text{EDA}\text{I}_2/\text{GlyHCl}$ -treated, **c**, $\text{EDA}\text{I}_2/\text{GlyHCl}$ -treated without PEDOT:PSS and **d**, Control perovskite films. Noting that, the size of Cl^- is even smaller than that of I^- within the perovskite composition. Thus, Cl^- is highly mobilizable in the whole wet process of the film fabrication. Additionally, Cl^- is too small to be composed to the perovskite structure in this case, it is therefore expelled out of the perovskite structures, and ends up at the grain surfaces, especially the top the bottom surfaces of the resultant films.

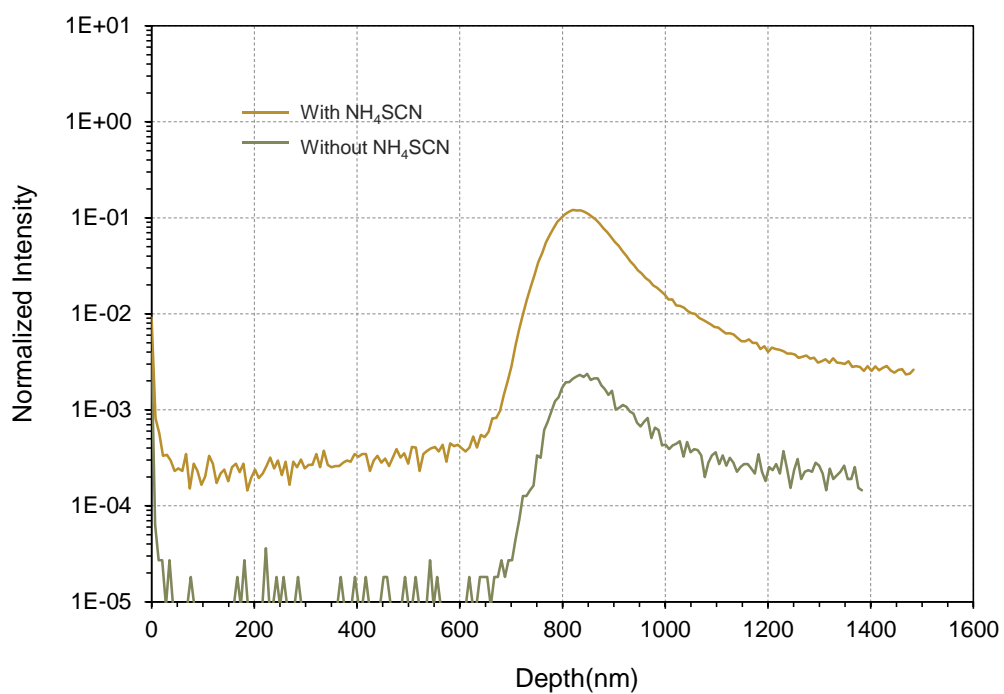


Fig. S16. ToF-SIMS depth profile of SCN⁻ ions in the perovskite films prepared with and without the addition of NH₄SCN.

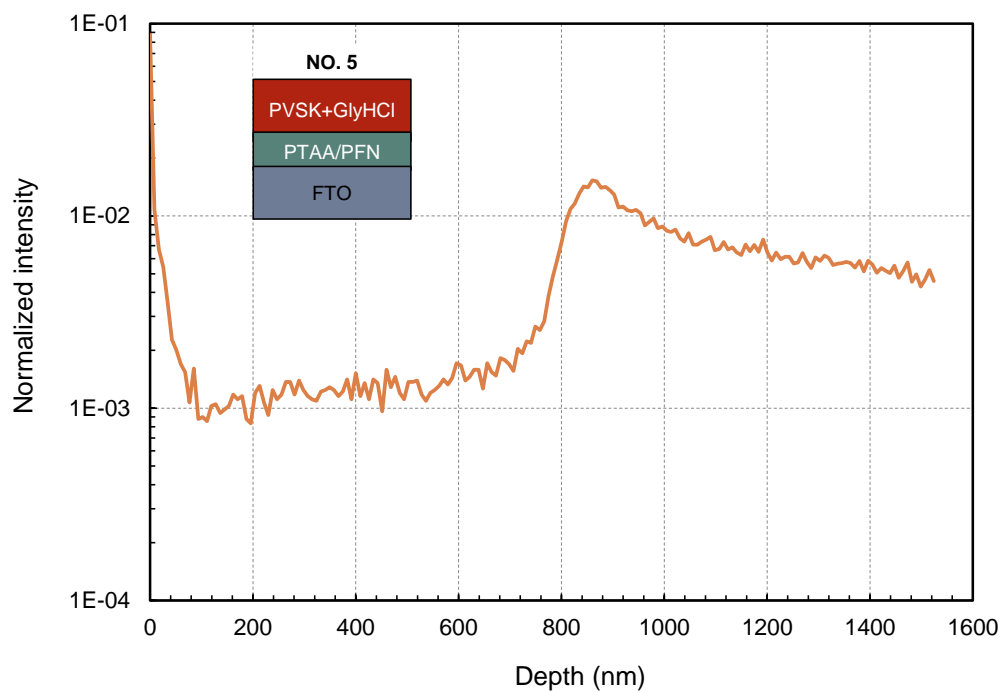
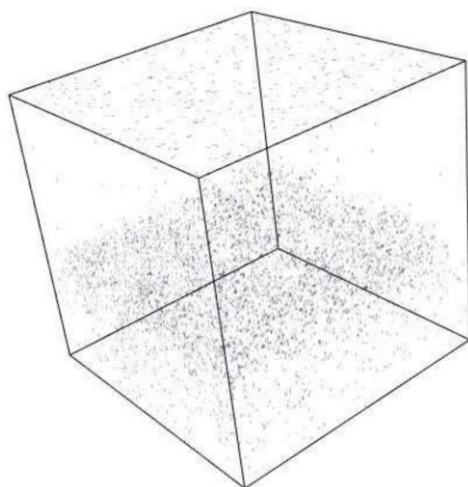


Fig. S17. ToF-SIMS depth profile of SCN^- ions in the perovskite films fabricated on PTAA/PFN-coated FTO substrates.

a



b

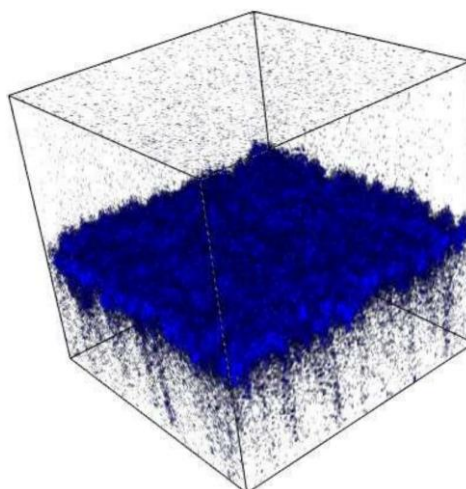


Fig. S18. Reconstructed 3D map (stretched in the z direction for clarity) showing the distributions of SCN⁻ ions in the perovskite films prepared without **a**, and with **b**, the addition of NH₄SCN.

A perovskite precursor solution containing 20 mol% GlyHCl was rapidly injected into the chlorobenzene antisolvent under vigorous stirring, forming black perovskite crystallites (Fig. S19a). The crystallites were collected and dried under vacuum, before re-dissolving them in dimethyl sulfoxide- d_6 and measuring the ^1H NMR spectrum. Signals from GlyH $^+$ could be identified, in addition to those from FA $^+$ and MA $^+$ (Fig. S19b). By comparing the integrated peak areas, the ratio of GlyH $^+$ against the total of A site component (Cs $^+$, FA $^+$, MA $^+$) was estimated to be 0.20. Assuming all the materials bind as a full coverage monolayer to the perovskite surfaces, an analysis of the surface/volume ratios suggests this would correspond to the formation of ca. 20 nm nanocrystals. More importantly, we note that the hydrogen atoms from the ammonium head of GlyH $^+$ are shifted by 0.32 ppm compared with the pristine GlyHCl (Fig. S19c), indicating that the ammonium group of GlyH $^+$ cation has an affinity for the perovskite components.

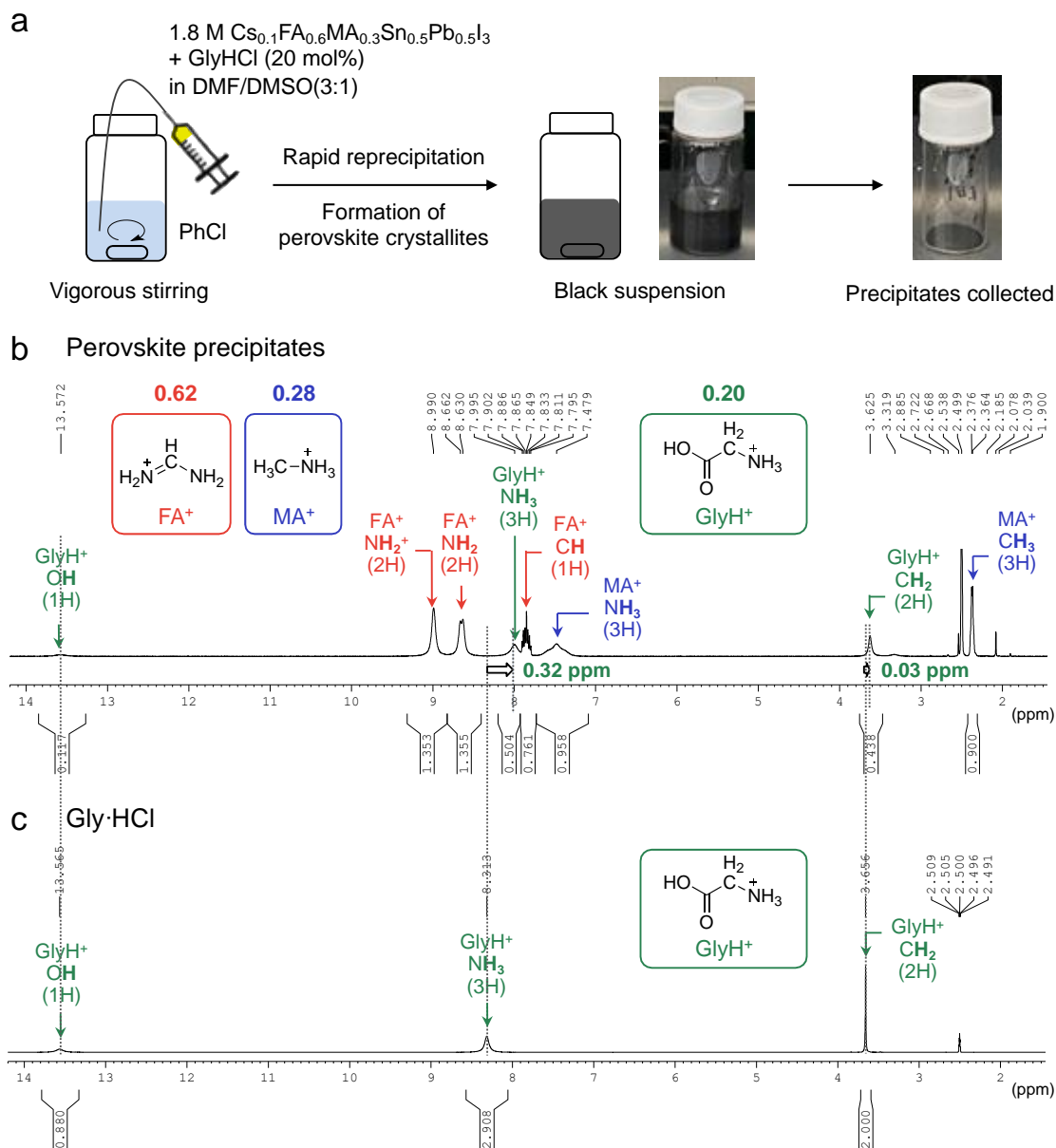


Fig. S19. Model experiments for the elucidation of the effect of GlyH⁺ in the perovskite crystallization process. **a**, Formation of perovskite crystallites by rapid reprecipitation. **b**, ¹H NMR spectrum of the perovskite crystallites in DMSO-*d*₆. **c**, Comparison with the spectrum of glycine hydrochloride (GlyHCl).

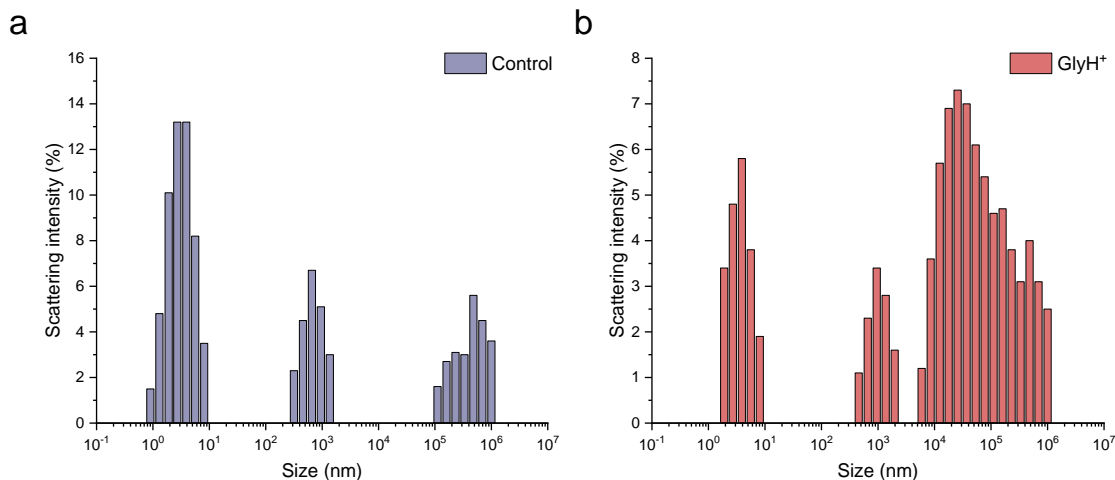


Fig. S20. Dynamic light scattering (DLS) results for the perovskite precursor solutions prepared **a**, without and **b**, with the addition of 2 mol% GlyHCl. Note that the DLS experiment was conducted around five hours after the sample preparation, as the sample transporting to, and equipment adjustment in, the company (Otsuka Electronics Co., Ltd., Japan).

XRD characterization

To confirm the effect of GlyHCl on the enhancement of the film crystallinity, we also compared the XRD patterns of the films fabricated with the addition of 2, 4, and 8 mol% GlyHCl without EDA_2 post-treatment. The intensity of the (100) peak increases with the amount of GlyHCl added into the precursor solution, and no new peaks or peak-shifts can be observed. We can therefore conclude that GlyHCl enhances the crystallinity of the resultant perovskite films without inducing new crystalline phases, such as the low dimension perovskite crystals.

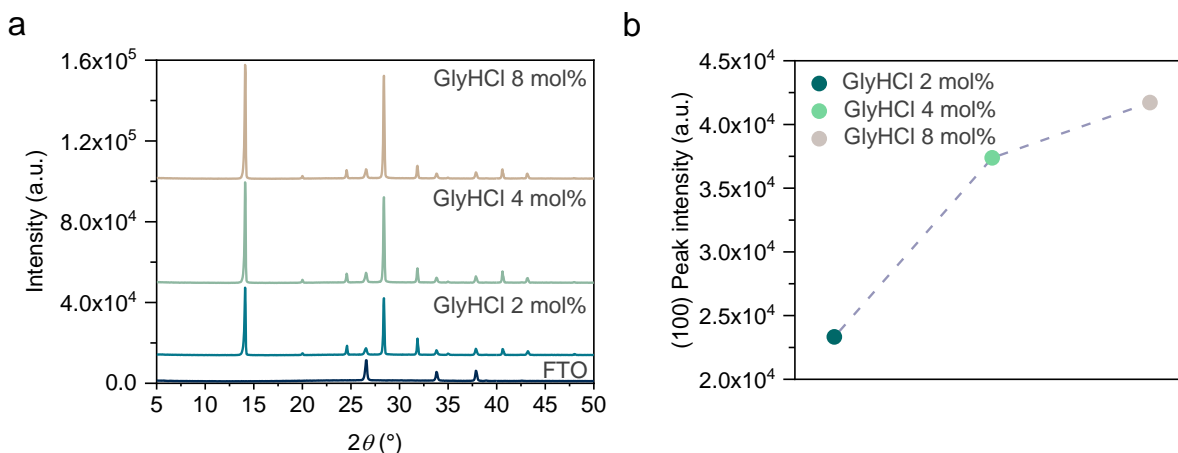


Fig. S21. **a**, XRD patterns of perovskite films prepared with the addition of 2, 4, and 8 mol% of GlyHCl (without EDA_2 post-treatment); **b**, the corresponding peak intensity of the (100) peaks.

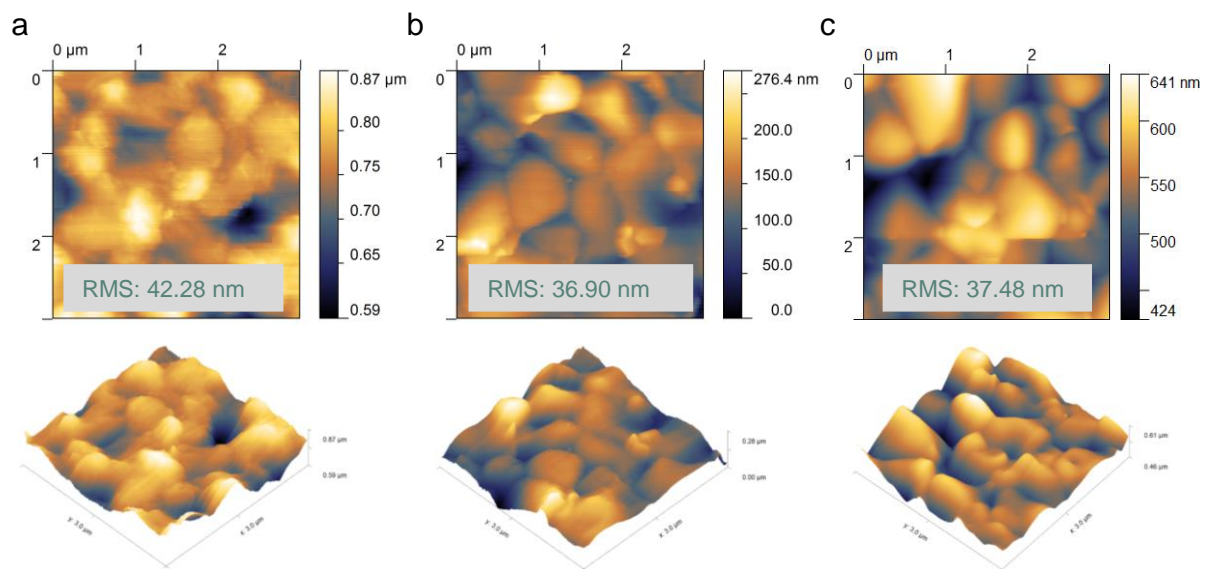


Fig. S22. AFM images of the **a**, control, **b**, EDAI₂-treated, and **c**, EDAI₂/GlyHCl-treated perovskite films.

Surface treatment

The composition of the co-solvent system (isopropanol and toluene with the volume ratio of 1:1) used for the EDAI_2 post-treatment is very important. The polarity of the isopropanol helps the organic ammonium salts to anchor to the film surface, enhancing defect passivation². Sn-containing perovskites are soluble in isopropanol³, however, so toluene was applied to reduce the overall viscosity of the solution to accelerate the dispersion of the EDAI_2 solution on the films before spinning. The viscosity of isopropanol and toluene is 2.40 and 0.59, respectively.

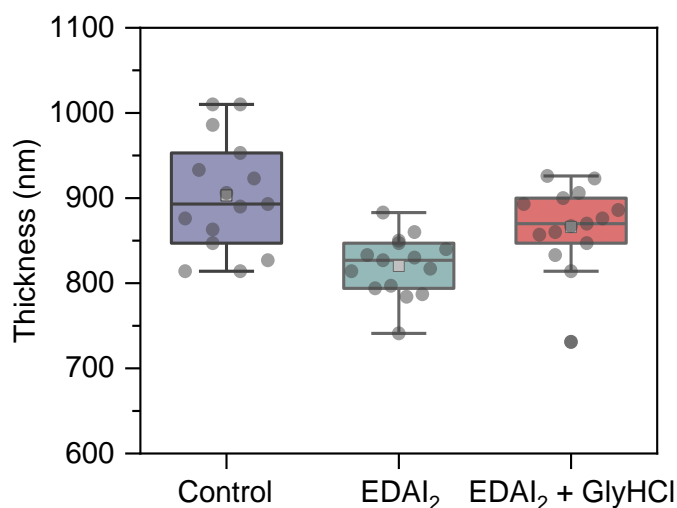


Fig. S23. Variations of the film thickness measured from 15 different cross-sections for each sample. The average thickness of the perovskite films is 870, 830, and 860 nm for control, EDAI_2 -treated, $\text{EDAI}_2/\text{GlyHCl}$ -treated perovskite films, respectively. The EDAI_2 -treated film is notably thinner than the control, this phenomenon also can be observed in the sample prepared for the SCLC characterizations (Table S2), confirming the polishing effect of the post-treatment with EDAI_2 solution.

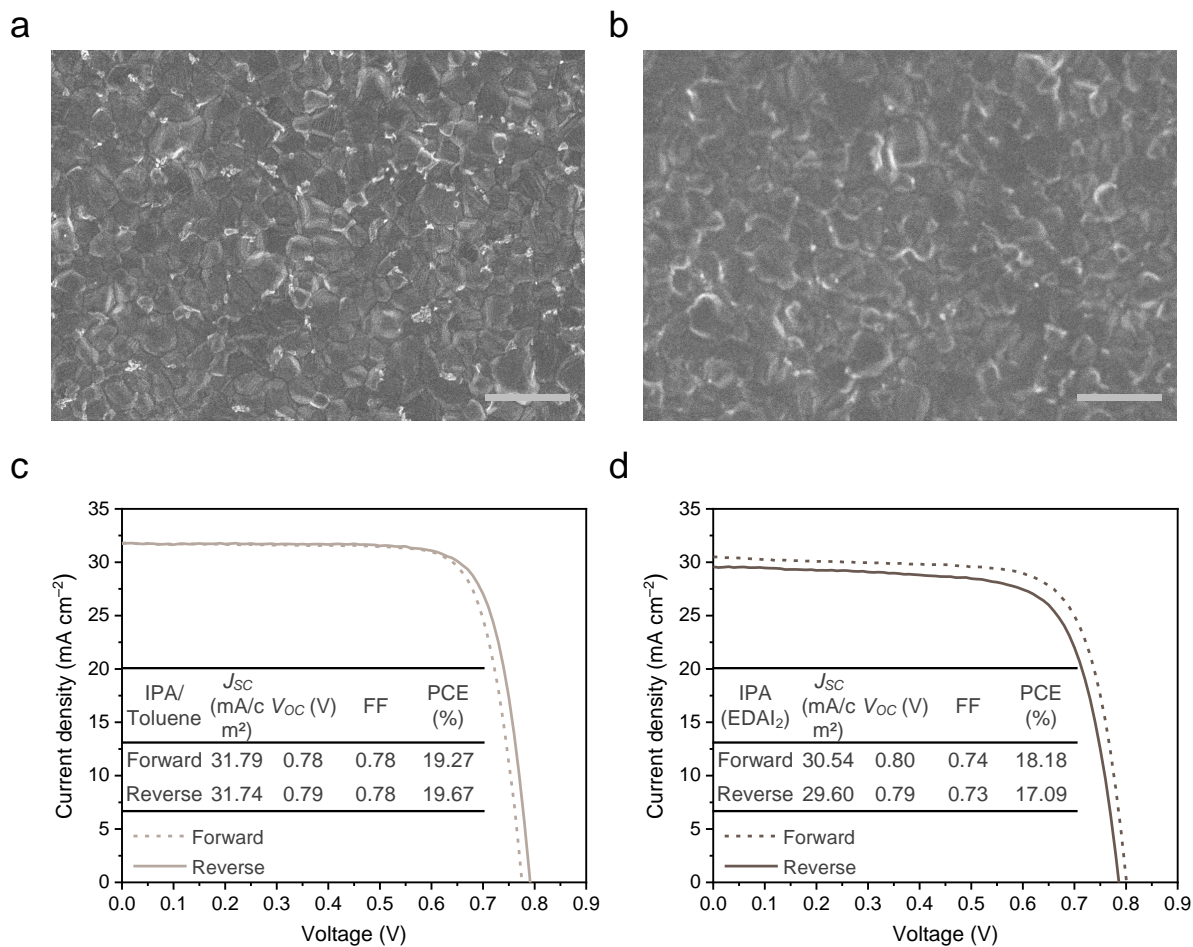


Fig. S24. Top-view (scale bar: 2 μm) SEM images of the control perovskite films treated with **a**, co-solvent and **b**, EDAI₂ in pure IPA solution fabricated on PEDOT:PSS-coated FTO/glass substrates. J - V curves of the devices fabricated with the control perovskite films treated with **c**, co-solvent and **d**, EDAI₂ in pure IPA solution.

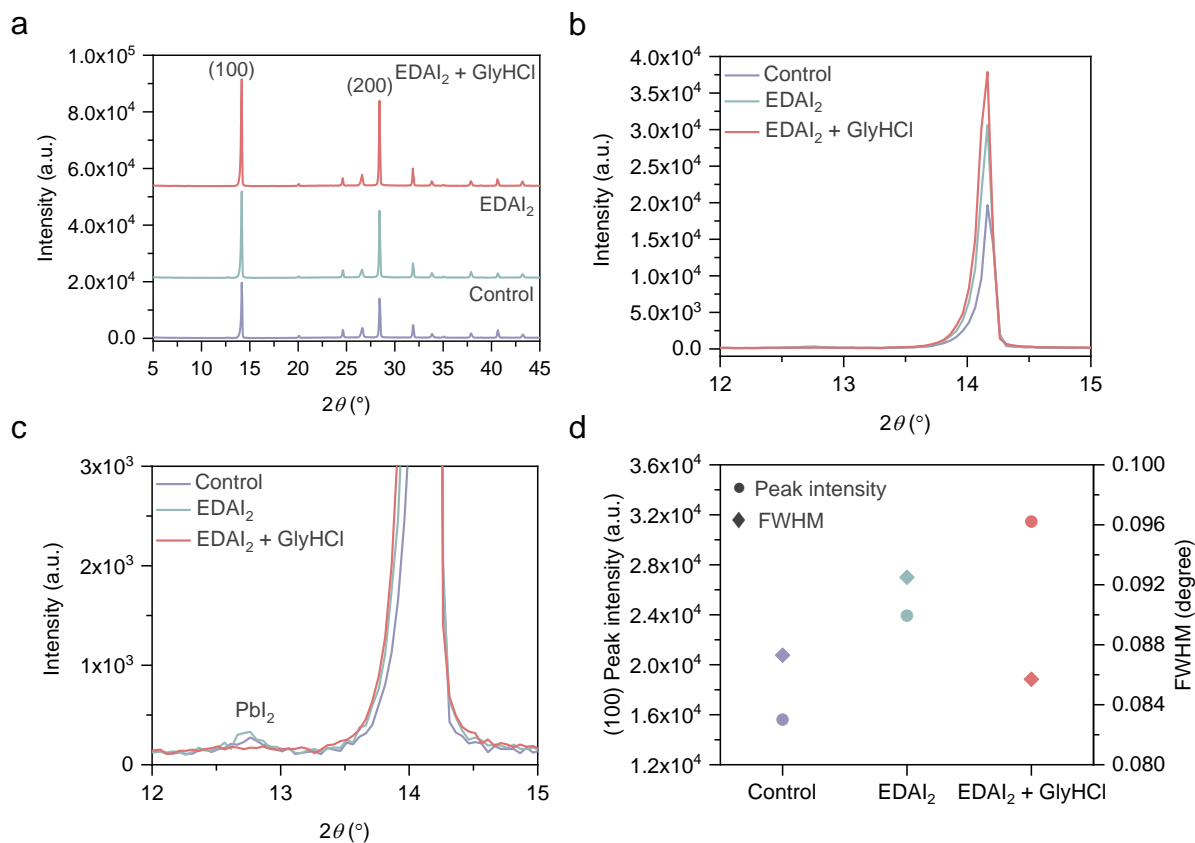


Fig. S25. XRD patterns of perovskite films with the 2θ range from **a**, 5 to 45°, **b**, 12 to 15° for showing the difference of the (100) peak intensity of the films, **c**, 12 to 15° with magnification for showing the PbI₂ peaks; **d**, the corresponding peak intensity and full width at half maximum (FWHM) of the (100) peaks. All diffraction peaks of FTO are indexed following the rutile tetragonal crystalline phase of SnO₂ (COD No. 96-210-1854). A thin layer of PMMA was coated onto the perovskite films to prevent oxidation.

To further investigate the structural characters at the film surface, we conducted grazing incidence XRD (GIXRD) measurements with incident angles of 0.2, 0.4, and 1.0° (Fig. S26 and 27). As the incident angle increases, more structural information is collected from regions further away from the top surface of the perovskite layer. As incident angle increased, the interplanar space in the crystal lattice of the films with treatments (Fig. S26a and b) expanded, indicating that the film at the surface region is more compressed than the bulk⁴. For the films fabricated with different modifications, the intensity of the (100) peaks increases especially with the incident angle of 0.2° (Fig. S26d), confirming the benefits of the treatments on the film crystallinity, particularly at the surface region.

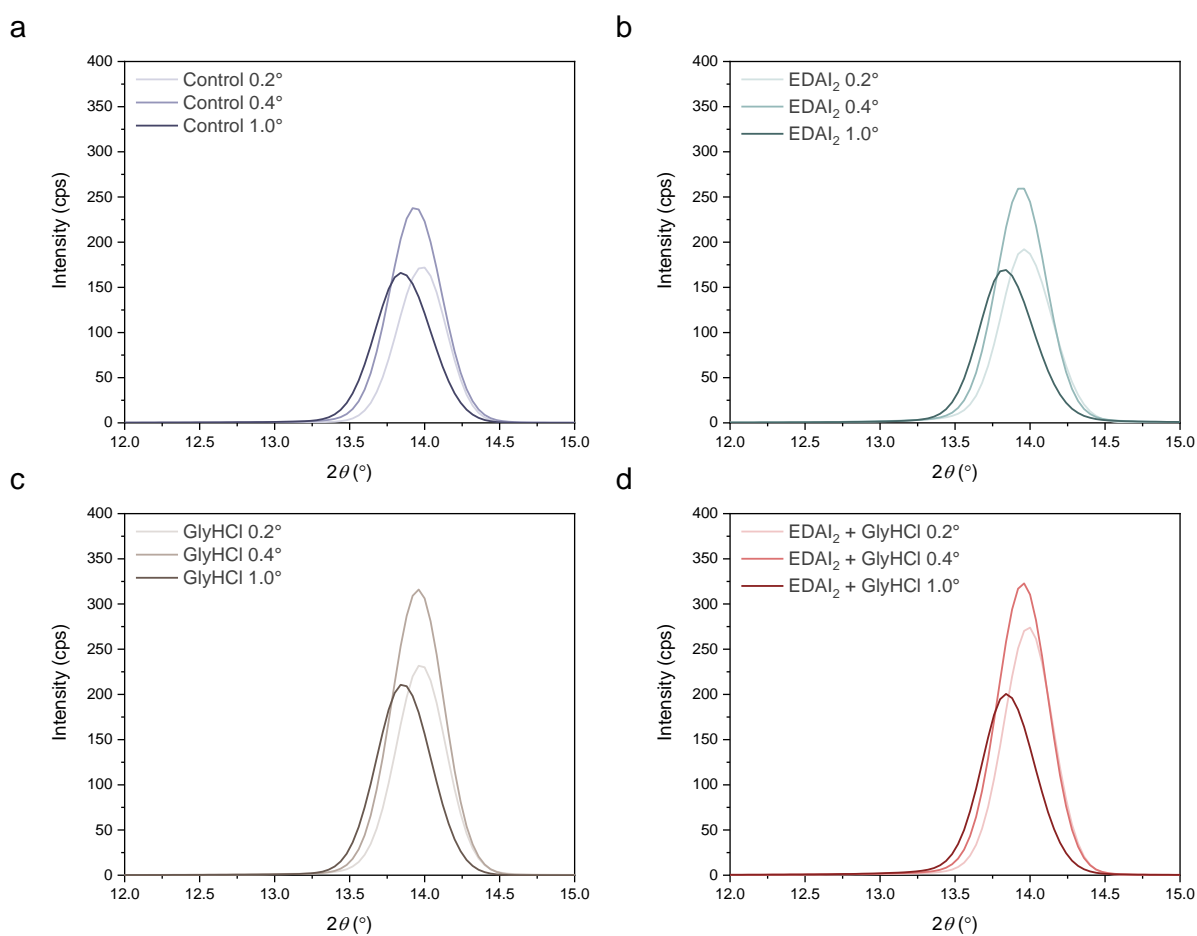


Fig. S26. Grazing incidence XRD patterns of **a**, control, **b**, EDAI₂-treated, **c**, GlyHCl-treated, and **d**, EDAI₂/GlyHCl-treated perovskite films measured with the incident angles of 0.2, 0.4, and 1.0°.

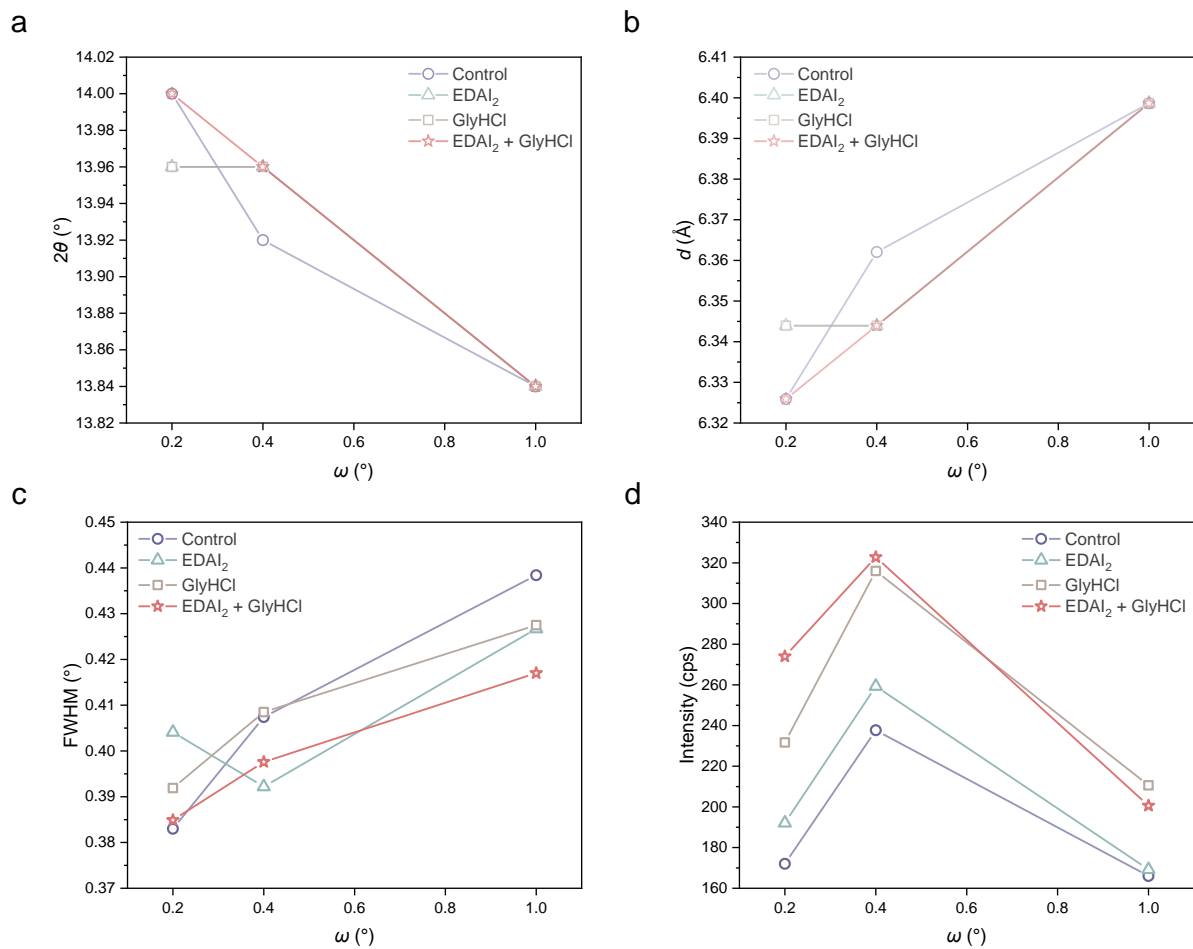


Fig. S27. Variations of 2θ , interplanar space (d), FWHM, and intensity of (100) peaks for the perovskite films measured with different incident angles (ω).

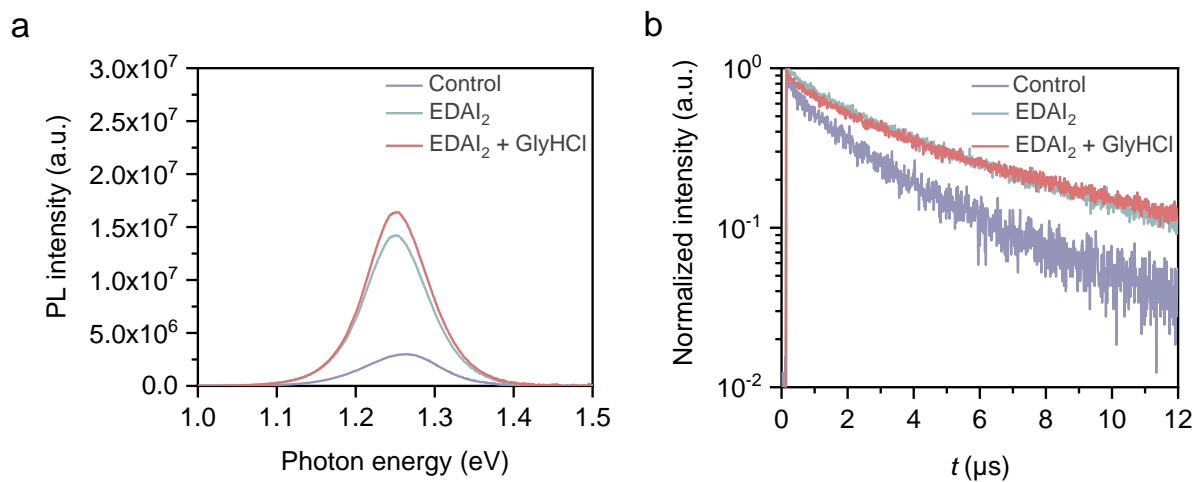


Fig. S28. a, Steady-state photoluminescence (PL) spectra of the perovskite films fabricated on quartz substrates with the front-side excitation. **b,** Time-resolved photoluminescence (TRPL) decay of the perovskite films fabricated on quartz substrates with the front-side excitation.

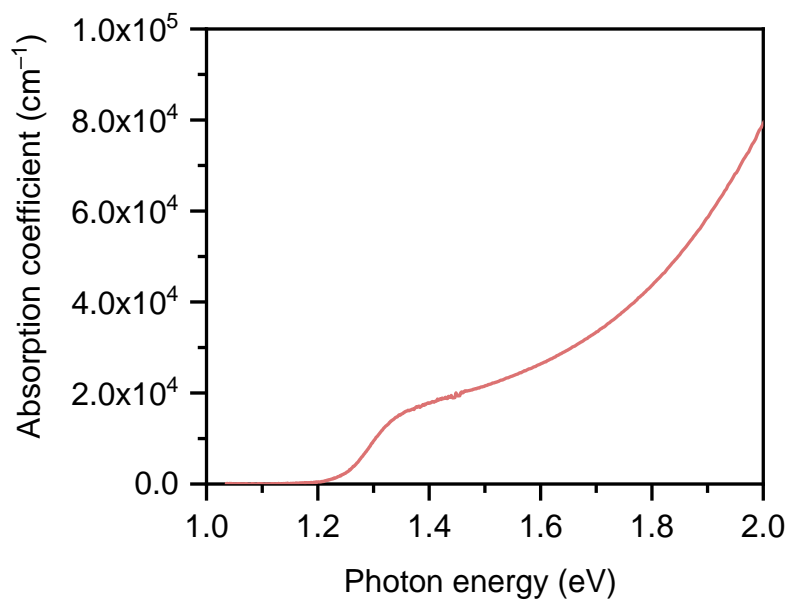


Fig. S29. Optical absorption spectrum of the EDAI₂/GlyHCl-treated perovskite film on quartz substrate.

Table S1. The PL lifetime, PL intensity, peak energy, and FWHM of the PL peaks for the perovskite films fabricated on quartz substrates.

Front-side excitation (Film surface side)	PL lifetime (μs)	PL intensity (a.u.)	Peak energy (eV)	FWHM (meV)
Control	2.8	2.99×10^6	1.261	112.1
EDAI ₂	4.5	1.42×10^7	1.251	94.95
EDAI ₂ + GlyHCl	4.9	1.64×10^7	1.252	93.58
Back-side excitation (Quartz side)	PL lifetime (μs)	PL intensity (a.u.)	Peak energy (eV)	FWHM (meV)
Control	1.5	2.43×10^6	1.246	104.7
EDAI ₂	3.2	1.29×10^7	1.251	102.9
EDAI ₂ + GlyHCl	5.5	2.12×10^7	1.244	98.67

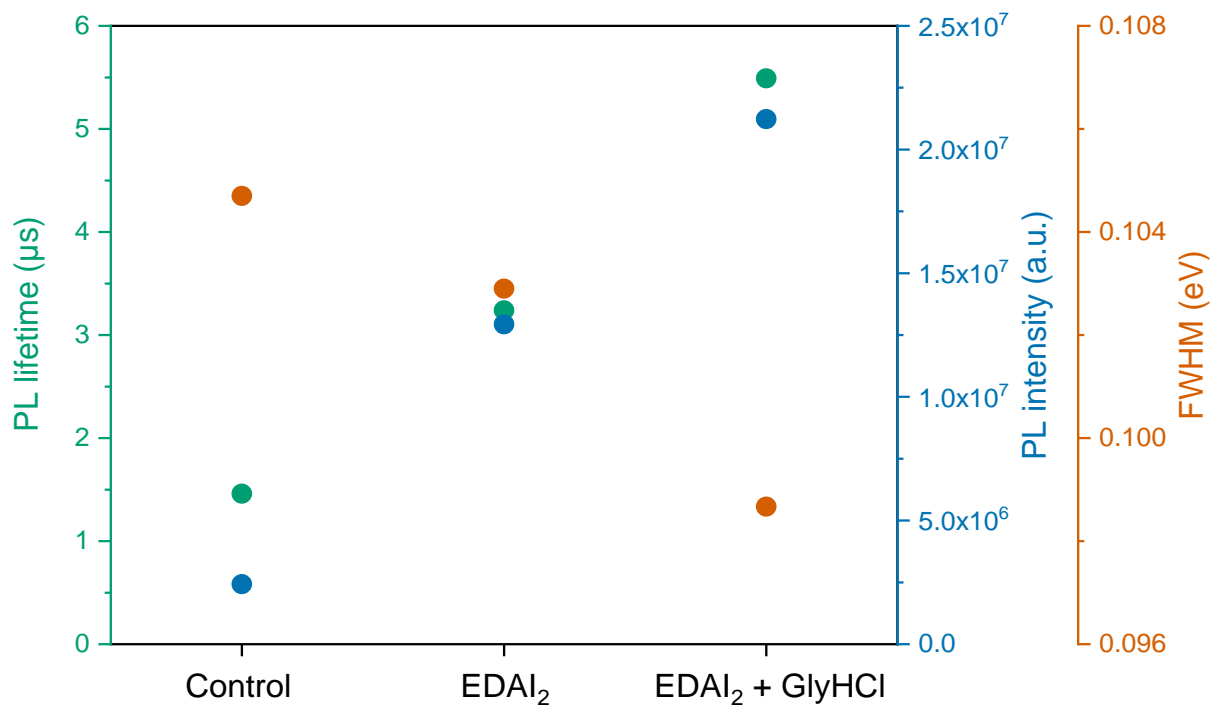


Fig. S30. The PL lifetime, PL intensity, and FWHM of the PL peaks for the perovskite films fabricated on quartz substrates with back-side excitation.

PL dynamics

At the range of excitation intensities under consideration here, the dependences of PL decay curves, PL lifetimes, and initial PL intensities shown in Fig. 2c, d, S31 are well explained by a simple rate equation that includes single-carrier trapping and two-carrier (electron–hole) radiative recombination¹:

$$\frac{dn}{dt} = -An - Bn^2 \quad (1)$$

$$I_{\text{PL}} \propto BnN + Bn^2 \quad (2)$$

Here n and I_{PL} are the photoexcited carrier density and the PL intensity, respectively. A , B , and N are the carrier trapping rate, the two-carrier radiative recombination coefficient, and the unintentional doped carrier density, respectively. Note that photoexcitation produces equal numbers of electrons and holes. The initial photoexcited carrier density $n(t=0) = n_0$ is given as follows:

$$n_0 = \alpha F_{\text{ex}} = \frac{\alpha \lambda}{hc} I_{\text{ex}} \quad (3)$$

Here h , c , λ , α , I_{ex} , and F_{ex} are the Planck constant, the speed of light, the excitation wavelength, the absorption coefficient at the excitation wavelength, the excitation fluence, and the excitation photon flux, respectively. In our TR-PL experiments, $\lambda = 688$ nm and $\alpha = 4.4 \times 10^4$ cm⁻¹. The excitation fluence of $I_{\text{ex}} = 100$ nJ cm⁻² corresponds to $n_0 = 1.5 \times 10^{16}$ cm⁻³ and $F_{\text{ex}} = 3.5 \times 10^{11}$ photons cm⁻², comparable to the incident photon flux under AM1.5G.

By solving the rate equations, the time-dependent PL intensity can be obtained as follows:

$$I_{\text{PL}}(t) = I_0 \left(\frac{N}{N + n_0} \left(\frac{n(t)}{n_0} \right) + \frac{n_0}{N + n_0} \left(\frac{n(t)}{n_0} \right)^2 \right) \quad (4)$$

where

$$\frac{n(t)}{n_0} = \frac{e^{-At}}{1 + \frac{Bn_0}{A}(1 - e^{-At})} \quad (5)$$

and

$$I_0 = \xi(N + n_0)n_0 \quad (6)$$

Here, I_0 is the initial PL intensity, while ξ is a constant that dependent on several factors, including the detection efficiency and the charge carrier extraction efficiency. According to the global fitting using Eqs. (4)–(6), $A = 9.2 \times 10^4$ s⁻¹, $B = 2.0 \times 10^{-11}$ cm³ s⁻¹, and $N = 8.2 \times 10^{14}$ cm⁻³ are obtained

for the GlyHCl/EDAI₂-treated sample. The value of A is three orders of magnitude lower than that of MAPbI₃¹, suggesting that our films have a lower density of traps such as the structural defects and impurities. The value of B is one order of magnitude lower than that of MAPbI₃¹, probably because of the smaller bandgap energy of Sn–Pb perovskites. The obtained unintentionally-doped carrier density N is similar to the reported values of MAPbI₃ ($\sim 10^{15} \text{ cm}^{-3}$)¹, suggesting that the characteristic p-doping commonly observed in Sn-containing perovskite materials is largely suppressed in our GlyHCl/EDAI₂-treated mixed Sn–Pb perovskite films.

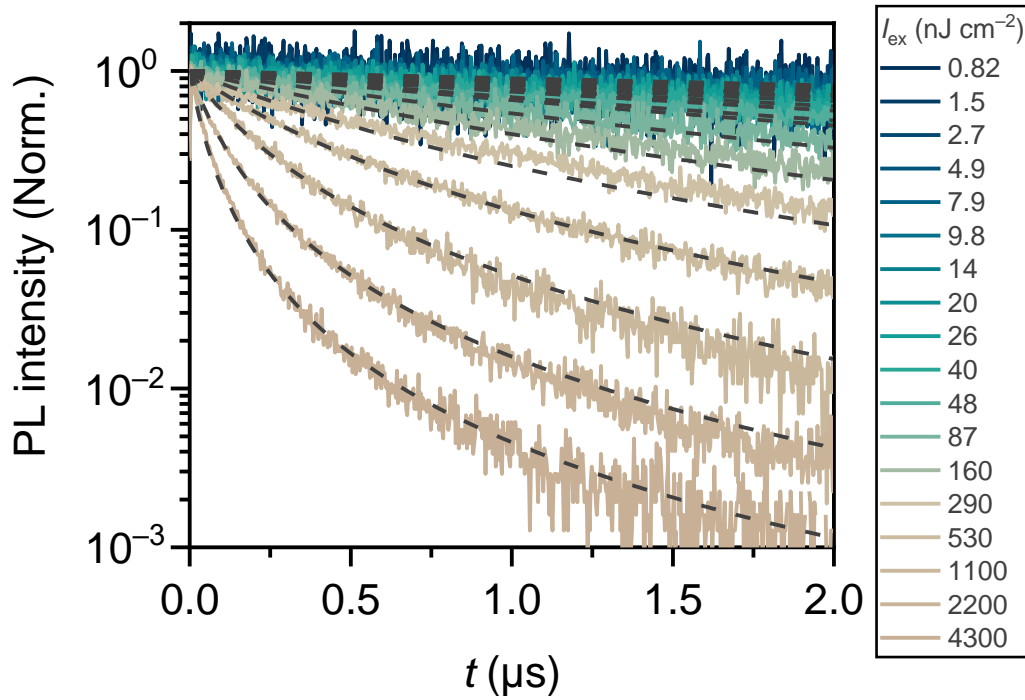


Fig. S31. PL dynamics of the EDAI₂/GlyHCl-treated films under different excitation intensities. Dashed lines represent the fit of the decay signals to the rate equations reported in our previous work¹.

Space-charge-limited currents (SCLC) characterization

Trap densities in the perovskite films were estimated from dark current–voltage (I – V) curves obtained for FTO/PEDOT:PSS/perovskite/PTAA/Ag hole-only, and FTO/C₆₀/perovskite/C₆₀/Ag electron-only devices^{5,6}. Fig. S32 shows the I – V curves of the hole-only devices. The voltages where the currents start to sharply increase can be assigned to the trap-filled limit voltage (V_{TFL}), from which the trap density, N_{trap} , can be estimated using the following relation: $V_{\text{TFL}} = N_{\text{trap}}(eL^2)/(2\epsilon_r\epsilon_0)$, where e is the elementary charge of the electron, ϵ_0 is the vacuum permittivity, ϵ_r is the relative dielectric constant of the perovskite (around 32)⁷, and L is the thickness of the perovskite film. The V_{TFL} values are given in Table S2. The estimated trap densities for the control, EDAI₂-treated, and EDAI₂/GlyHCl-treated films were 3.0×10^{15} , 2.9×10^{15} , and $1.7 \times 10^{15} \text{ cm}^{-3}$, respectively. The EDAI₂/GlyHCl-treated films have the lowest trap-state density, and therefore, the corresponding devices should have the smallest number of recombination events. Meanwhile, the EDAI₂/GlyHCl-treated films also showed a low density of electron traps ($2.9 \times 10^{14} \text{ cm}^{-3}$), as determined from the electron only devices.

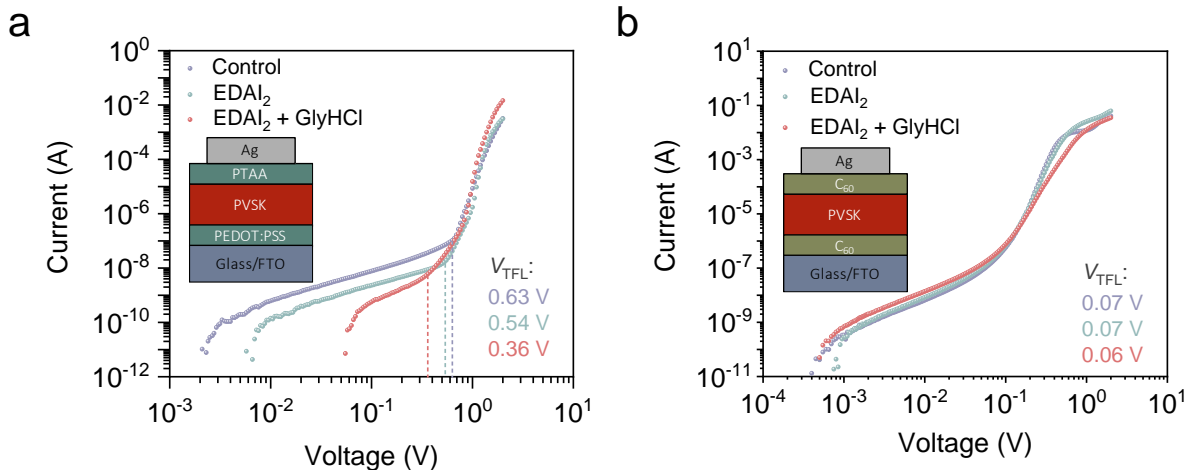


Fig. S32. Dark I – V curves of the **a**, hole-only and **b**, electron-only devices with the architectures of FTO/PEDOT:PSS/perovskite/PTAA/Ag and FTO/C₆₀/perovskite/C₆₀/Ag, respectively.

Table S2. The hole and electron trap densities estimated from the SCLC measurements.

Sample	Hole-only devices		N_{trap} (hole) (cm^{-3})	Electron-only devices		N_{trap} (electron) (cm^{-3})
	Thickness	V_{TFL}		Thickness	V_{TFL}	
	(nm)	(V)	(nm)	(V)		
Control	867	0.63	3.0×10^{15}	817	0.07	3.7×10^{14}
EDAI ₂	814	0.54	2.9×10^{15}	775	0.07	3.9×10^{14}
EDAI ₂ + GlyHCl	863	0.36	1.7×10^{15}	828	0.06	2.9×10^{14}

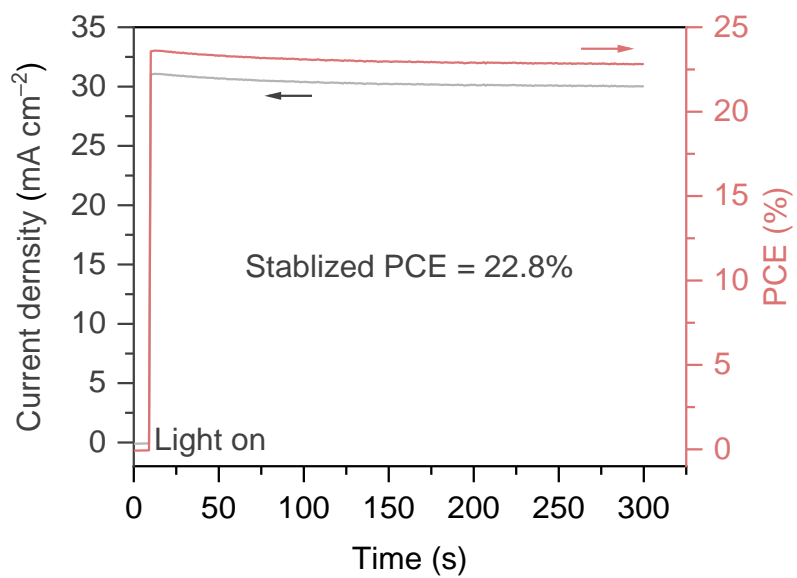


Fig. S33. Stabilized power output of the EDAI₂/GlyHCl-treated device measured by fixing the voltage at 0.76 V under AM1.5G.

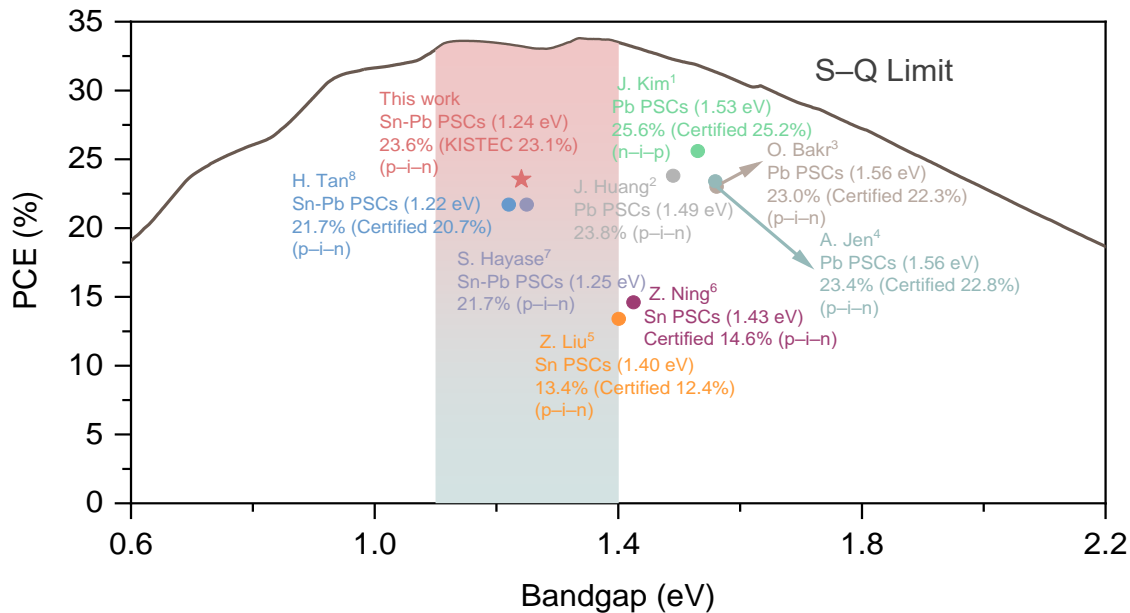
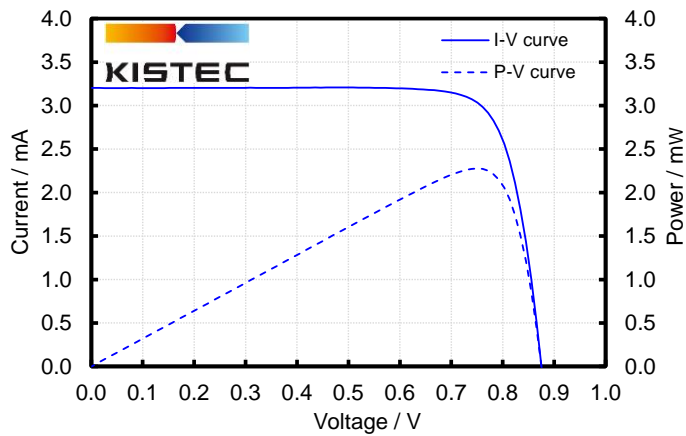


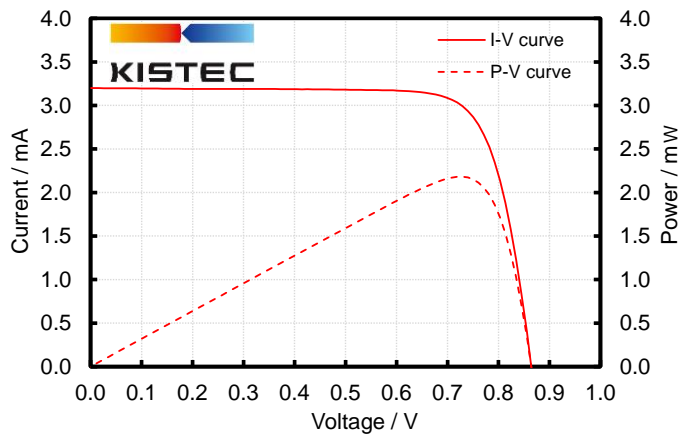
Fig. S34. Efficiencies of some representative PSCs. The bandgap from 1.1 to 1.4 eV is the optimal range for a single junction solar cell based on Shockley–Queisser theory⁸. Plotted PCEs are referred from **1**: J. Kim et al., *Nature* **2021**, 592, 381–385. Perovskite composition: α -FAPbI₃; **2**: J. Huang et al., *Science* **2021**, 373, 902–907. Perovskite composition: MAPbI₃; **3**: O. Bakr et al., *Nat. Energy* **2020**, 5, 131–140. Perovskite composition: Cs_{0.05}(FA_{0.92}MA_{0.08})_{0.95}Pb(I_{0.92}Br_{0.08})₃; **4**: A. K.-Y. Jen et al., *J. Am. Chem. Soc.* **2020**, 142, 20134–20142. Perovskite composition: Cs_{0.05}(FA_{0.95}MA_{0.05})_{0.95}Pb(I_{0.95}Br_{0.05})₃; **5**: Z. Liu et al., *Matter* **2021**, 4, 709–721. Perovskite composition: FASnI_{2.9}Br_{0.1}; **6**: Z. Ning et al., *J. Am. Chem. Soc.* **2021**, 143, 10970–10976. Perovskite composition: 2D/3D tin perovskite; **7**: S. Hayase et al., *Adv. Energy Mater.* **2021**, 11, 2101069. Perovskite composition: Cs_{0.025}FA_{0.475}MA_{0.5}Sn_{0.5}Pb_{0.5}I_{2.975}Br_{0.025}; **8**: H. Tan et al., *Nat. Energy* **2020**, 5, 870–880. Perovskite composition: FA_{0.7}MA_{0.3}Pb_{0.5}Sn_{0.5}I₃.



Date : 11 Mar 2021
 Cell name : HF2714-Right
 Start delay time : 100 ms
 Delay time : 10 ms
 Integration time : 10 ms
 Sweep direction : Reverse
 Designated area : 0.0985 cm²
 Isc : 3.203 / mA
 Voc : 0.875 / V
 Pmax : 2.278 / mW
 Ipm : 3.039 / mA
 Vpm : 0.750 / V
 F.F. : 81.2 / %
 Eff. : 23.1 / %
 M. Temp : R.T.

I-V curve and P-V curve

Fig. S35. Reverse scan of an unencapsulated cell measured by the Kanagawa Institute of Industrial Science and Technology (KISTEC).



Date : 11 Mar 2021
 Cell name : HF2714-Right
 Start delay time : 100 ms
 Delay time : 10 ms
 Integration time : 10 ms
 Sweep direction : Forward
 Designated area : 0.0985 cm²
 Isc : 3.200 / mA
 Voc : 0.864 / V
 Pmax : 2.183 / mW
 Ipm : 3.009 / mA
 Vpm : 0.725 / V
 F.F. : 79.0 / %
 Eff. : 22.2 %
 M. Temp : R.T.

I-V curve and P-V curve

Fig. S36. Forward scan of an unencapsulated cell measured by the Kanagawa Institute of Industrial Science and Technology (KISTEC).

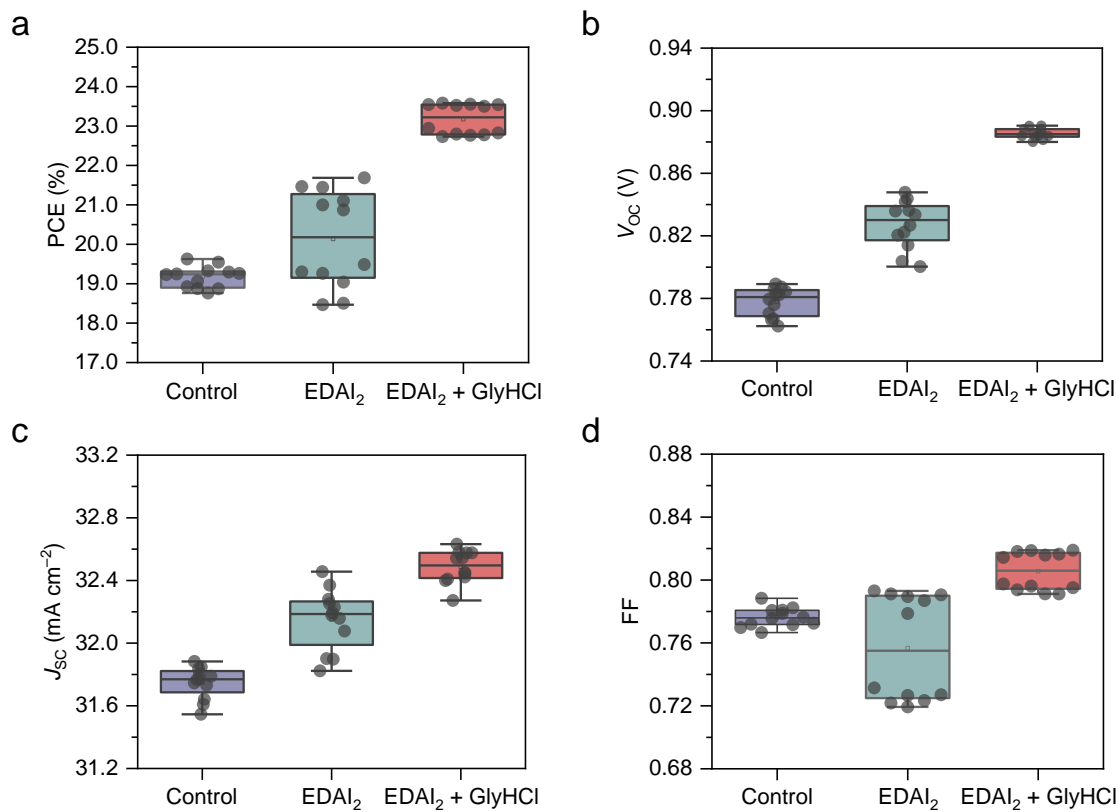


Fig. S37. Distributions of the device parameters derived from forward and reverse J - V scans for the control, EDAl₂-treated, and EDAl₂/GlyHCl-treated devices (six samples for each condition).

Table S3. Device performance parameters.

Sample	Scan ^a	J_{sc} (mA cm ⁻²)	V_{oc} (V)	FF	PCE (%)
Control	Forward	31.6	0.76	0.78	18.8
	Reverse	31.6	0.78	0.78	19.3
	Forward	31.8	0.77	0.78	19.1
	Reverse	31.8	0.79	0.78	19.5
	Forward	31.8	0.77	0.78	18.9
	Reverse	31.6	0.79	0.79	19.6
	Forward	31.8	0.77	0.77	18.9
	Reverse	31.8	0.78	0.77	18.9
	Forward	31.9	0.78	0.78	19.3
	Reverse	31.8	0.78	0.77	19.3
	Forward	31.9	0.78	0.77	19.3
	Reverse	31.7	0.79	0.77	19.2
	Forward (av.)	31.8 ± 0.1	0.77 ± 0.01	0.78 ± 0.00	19.1 ± 0.2
	Reverse (av.)	31.7 ± 0.1	0.79 ± 0.01	0.78 ± 0.01	19.3 ± 0.2
EDAI ₂	Forward	32.2	0.81	0.73	19.0
	Reverse	32.2	0.83	0.78	20.9
	Forward	31.9	0.80	0.72	18.5
	Reverse	31.8	0.84	0.79	21.0
	Forward	32.1	0.80	0.72	18.5
	Reverse	31.9	0.84	0.79	21.1
	Forward	32.5	0.82	0.72	19.3
	Reverse	32.4	0.84	0.79	21.4
	Forward	32.2	0.83	0.73	19.5
	Reverse	32.3	0.85	0.79	21.7
	Forward	32.3	0.82	0.73	19.3
	Reverse	32.2	0.84	0.79	21.5
	Forward (av.)	32.2 ± 0.2	0.81 ± 0.01	0.73 ± 0.01	19.0 ± 0.7
	Reverse (av.)	32.1 ± 0.2	0.84 ± 0.01	0.79 ± 0.00	21.3 ± 0.3
EDAI ₂ + GlyHCl	Forward	32.5	0.88	0.79	22.8
	Reverse	32.4	0.89	0.82	23.6
	Forward	32.4	0.88	0.80	22.8
	Reverse	32.3	0.89	0.82	23.5
	Forward	32.6	0.88	0.79	22.8
	Reverse	32.4	0.89	0.82	23.5
	Forward	32.5	0.88	0.79	22.7
	Reverse	32.5	0.89	0.82	23.6
	Forward	32.6	0.88	0.80	22.8
	Reverse	32.5	0.89	0.82	23.5
	Forward	32.6	0.88	0.80	22.9
	Reverse	32.6	0.89	0.81	23.5
	Forward (av.)	32.5 ± 0.1	0.88 ± 0.00	0.79 ± 0.01	22.8 ± 0.1
	Reverse (av.)	32.5 ± 0.1	0.89 ± 0.00	0.82 ± 0.00	23.5 ± 0.0

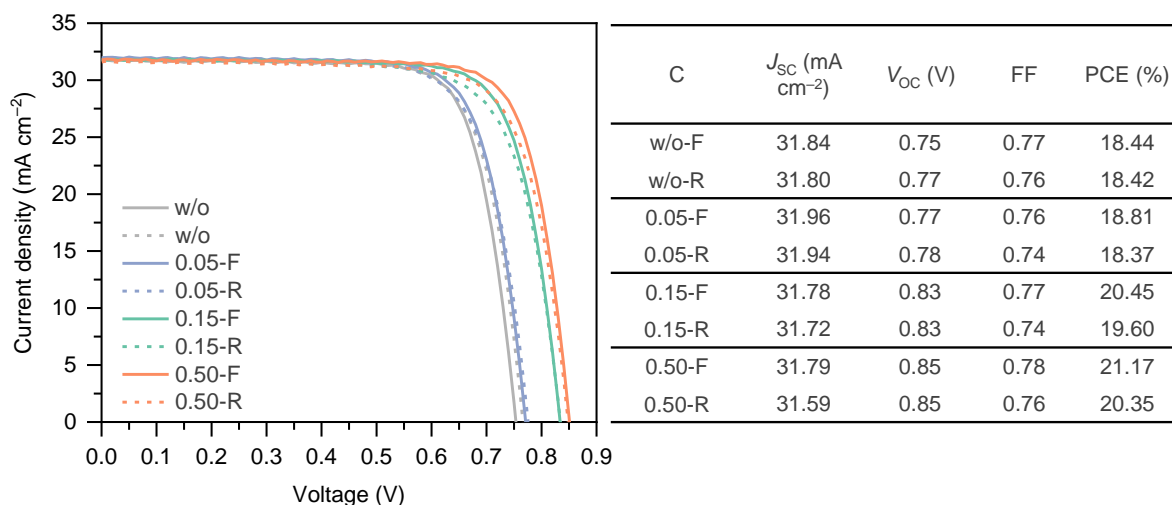


Fig. S38. The J - V curves and the device performance parameters of the solar cells fabricated within the same batch. w/o, 0.05, 0.15, and 0.50 represent the perovskite films treated with the solution prepared without EDAI_2 , and with 0.05, 0.15, 0.50 mg EDAI_2 into 1 mL IPA/toluene (v:v = 1:1), respectively. A saturated solution with a concentration of about 0.3 mg mL^{-1} EDAI_2 formed when 0.50 mg EDAI_2 was added.

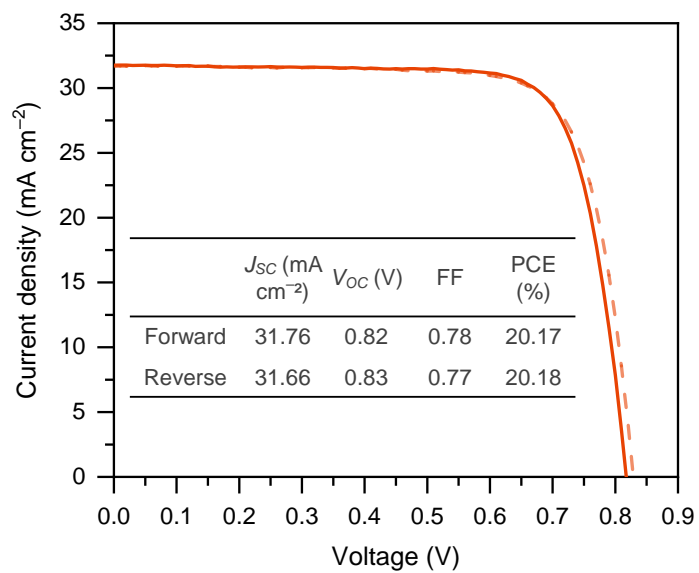


Fig. S39. Representative J - V curves of the device fabricated with the addition of 2 mol% GlyHCl while without EDAI₂ treatment.

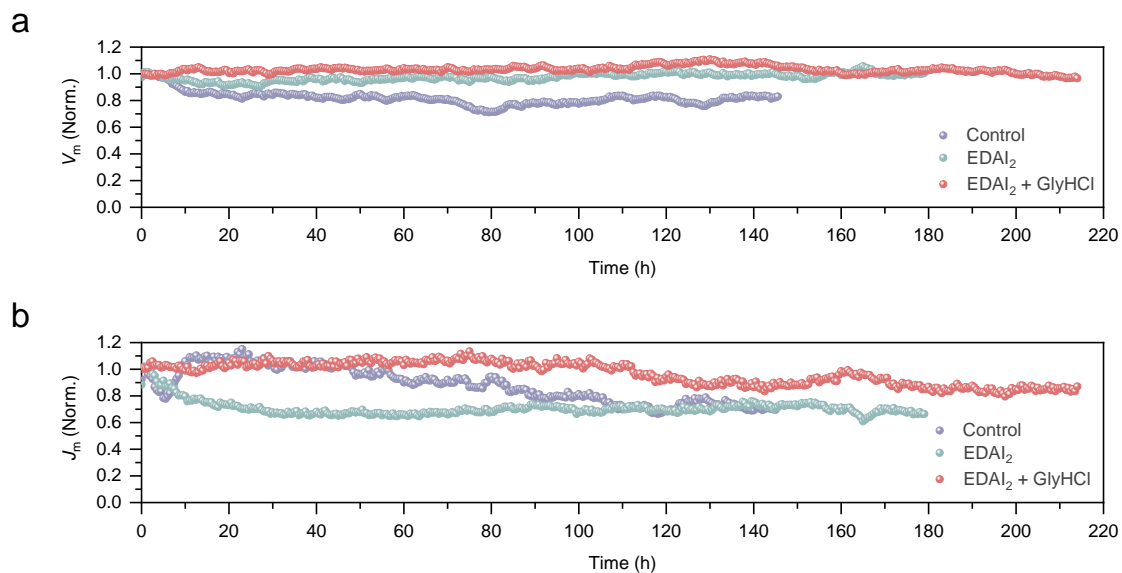


Fig. S40. Output voltages, **a**, and currents, **b**, obtained from the maximum power point tracking (MPPT) for the control, EDAI₂-treated, and EDAI₂/GlyHCl-treated cells measured without encapsulation in a N₂-filled glovebox under AM1.5G simulated solar illumination. The MPPT data were given in Fig. 3e. The loss of PCE over time is mainly caused by the drop of output current, the output voltages remain relatively stable.

Table S4. Device performance parameters of nine large area PSCs with 1 cm² active device area.

Scan ^a	J_{SC} (mA cm ⁻²)	V_{OC} (V)	FF	PCE (%)
Forward	32.02	0.88	0.70	19.7
Reverse	31.6	0.87	0.69	19.1
Forward	31.8	0.87	0.69	19.2
Reverse	31.5	0.87	0.68	18.5
Forward	32.2	0.88	0.68	19.1
Reverse	31.9	0.87	0.67	18.5
Forward	32.0	0.88	0.70	19.6
Reverse	31.5	0.87	0.69	19.0
Forward	33.1	0.88	0.72	21.0
Reverse	32.4	0.88	0.72	20.3
Forward	32.2	0.88	0.73	20.5
Reverse	31.6	0.87	0.72	19.8
Forward	32.1	0.88	0.72	20.3
Reverse	31.5	0.87	0.71	19.6
Forward	32.5	0.88	0.72	20.6
Reverse	31.6	0.88	0.72	19.9
Forward	33.7	0.87	0.67	19.6
Reverse	31.5	0.86	0.75	20.4
Forward (av.)	32.4 ± 0.6	0.87 ± 0.00	0.70 ± 0.02	20.0 ± 0.6
Reverse (av.)	32.7 ± 0.3	0.87 ± 0.01	0.71 ± 0.02	19.5 ± 0.7

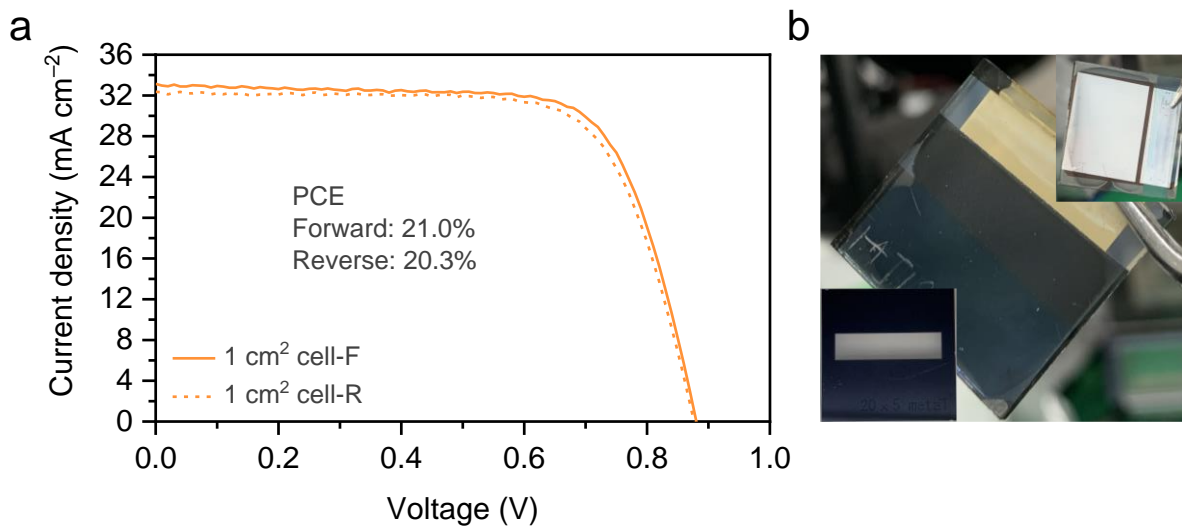


Fig. S41. a, J - V curves for the best performing large area device, with an active area 1 cm^2 . The PCE is 21.0% for the forward scan ($J_{\text{SC}} = 33.1 \text{ mA cm}^{-2}$, $V_{\text{OC}} = 0.88 \text{ V}$, $\text{FF} = 0.72$). **b**, Photos of the cell with 1 cm^2 active area. Insets show the front side of the cell and the optical mask used for the measurement.

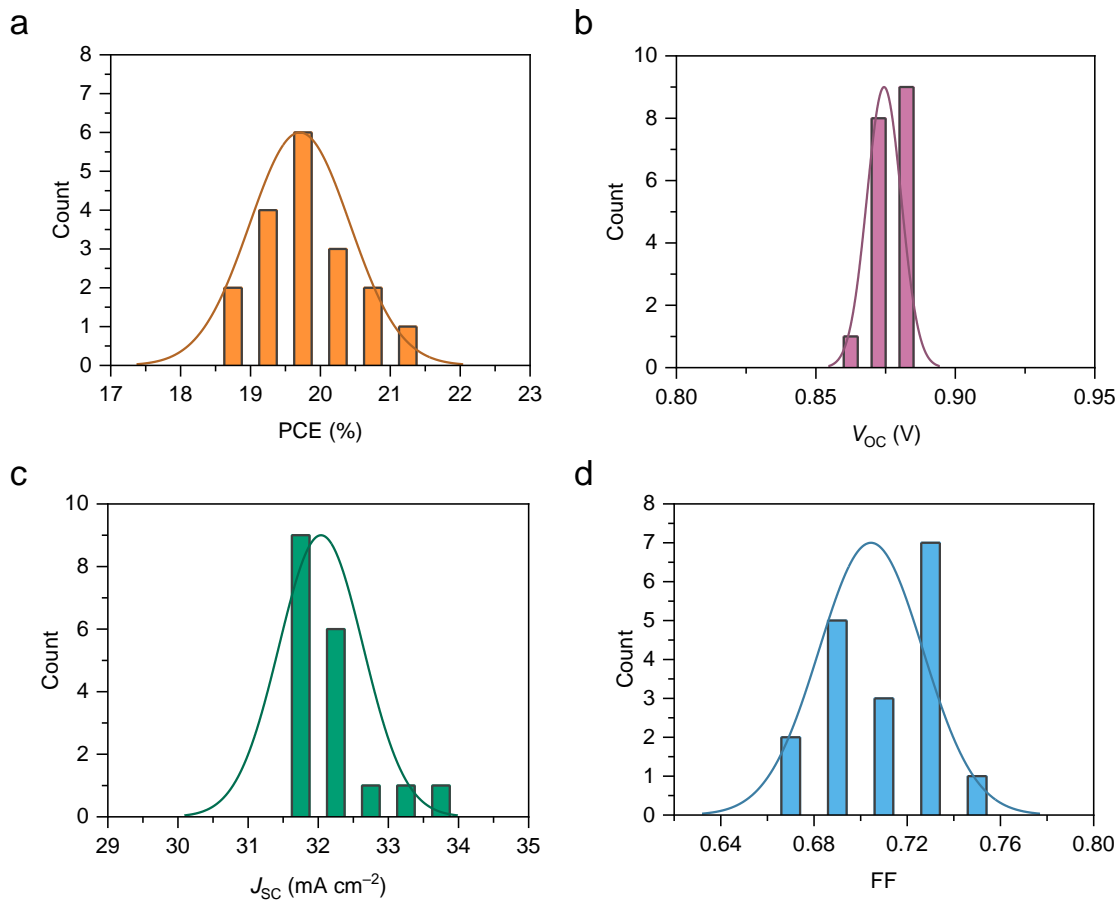


Fig. S42. Histograms of the J - V parameters obtained from nine devices with 1 cm^2 active area.

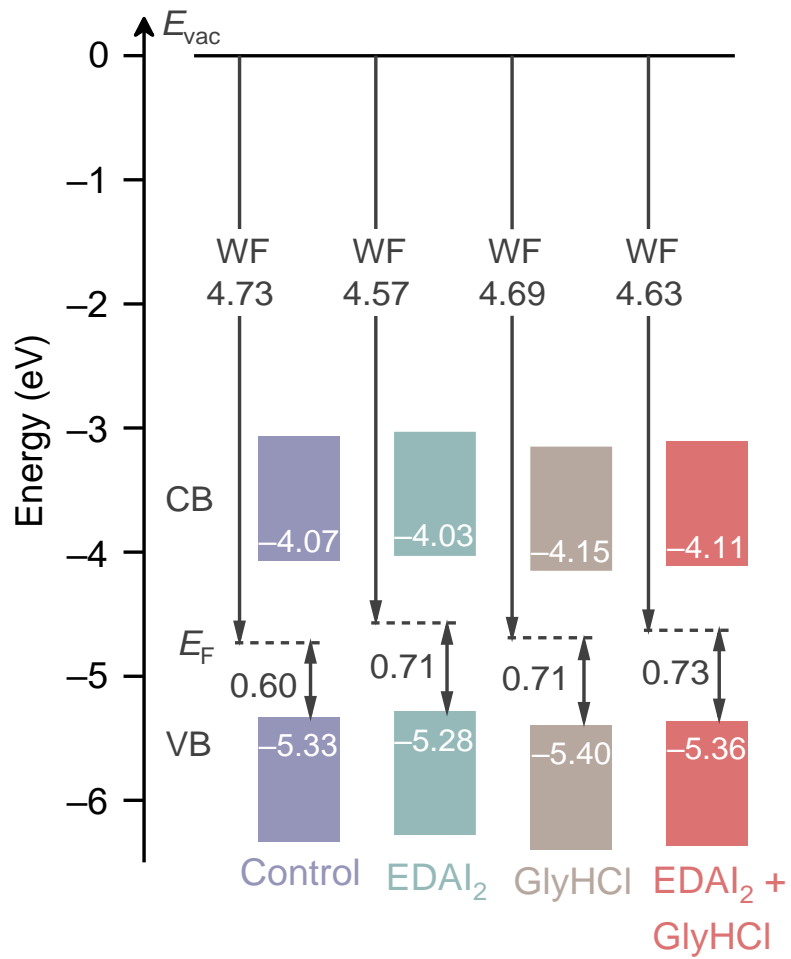


Fig. S43. Energy levels of the perovskite films. Energies are given in electron volts relative to vacuum level. The detailed UPS spectra were given in Fig. 4a and b.

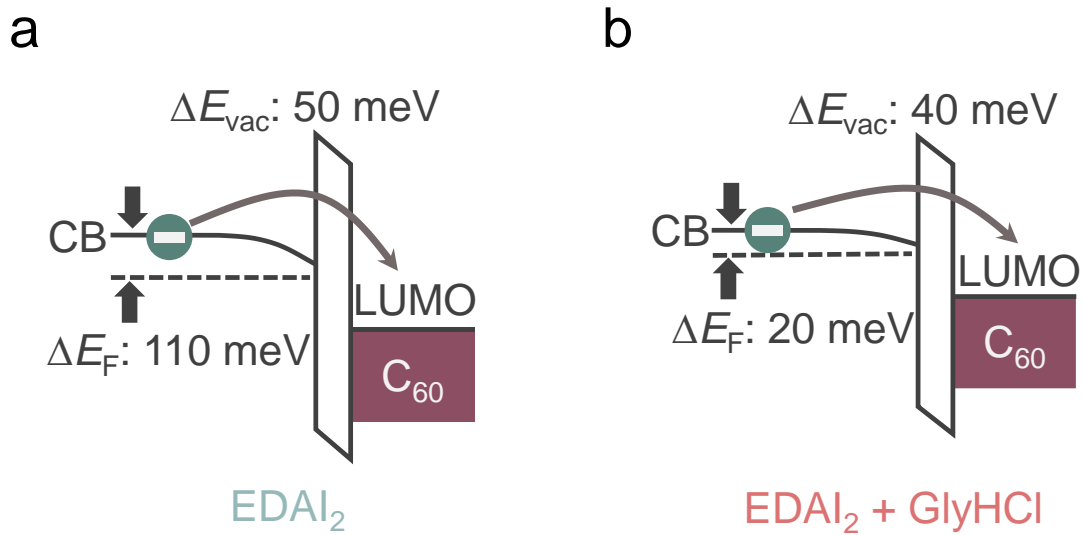


Fig. S44. Energy level shifts induced by EDAI₂ post-treatment for the perovskite layers prepared **a**, without GlyHCl additive and **b**, with GlyHCl additive.

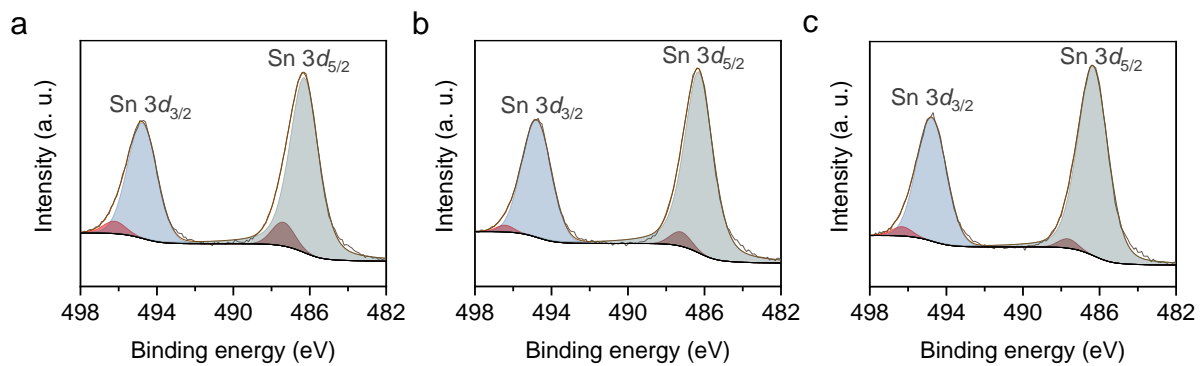


Fig. S45. XPS spectra of the Sn $3d_{3/2}$ and $3d_{5/2}$ core levels for the **a**, control, **b**, EDAI₂-treated, and **c**, EDAI₂/GlyHCl-treated perovskite films.

Table S5. The $\text{Sn}^{4+}/(\text{Sn}^{2+} + \text{Sn}^{4+})$ ratio and binding energy of the Sn^{4+} and Sn^{2+} peaks, as determined from the deconvolution of the $3d_{3/2}$ and $3d_{5/2}$ XPS peak manifolds shown in Fig. S45.

Sample	$\text{Sn}^{4+}/(\text{Sn}^{2+} + \text{Sn}^{4+})$ (%)	$3d_{3/2}$ (eV)		$3d_{5/2}$ (eV)	
		Sn^{4+}	Sn^{2+}	Sn^{4+}	Sn^{2+}
Control	8.5	496.23	494.77	487.39	486.29
EDAI ₂	4.1	496.43	494.78	487.24	486.30
EDAI ₂ + GlyHCl	3.9	496.32	494.77	487.66	486.35

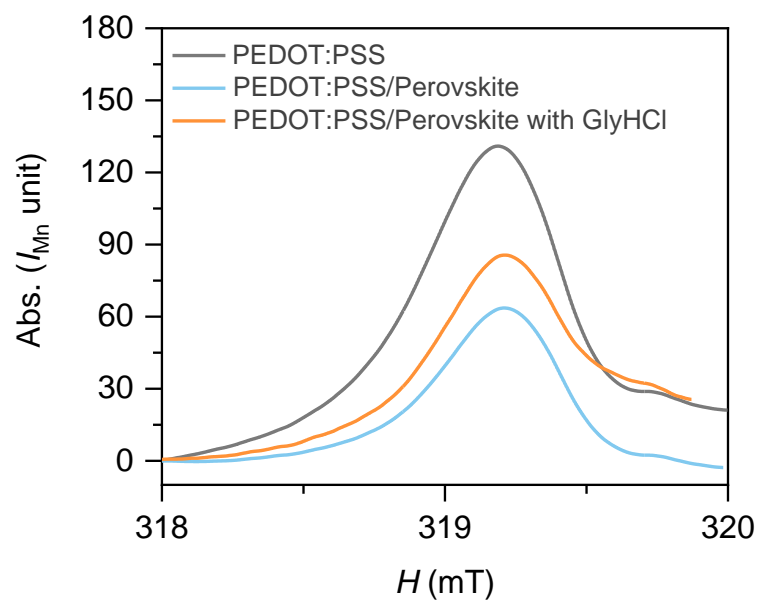


Fig. S46. The integrated ESR spectra for the data presented in Fig. 4d.

Table S6. The number of spins and spin densities for the three PEDOT:PSS samples.

Sample ^a	Number of spins	Spin density (cm ⁻³)
PEDOT:PSS	3.60×10^{13}	2.22×10^{19}
PEDOT:PSS/Perovskite	2.21×10^{13}	1.36×10^{19}
PEDOT:PSS/Perovskite + GlyHCl	2.39×10^{13}	1.47×10^{19}

^aThe films were fabricated on quartz substrates.

Further detail about the filming processes for better lab-to-lab reproducibility

We observed white dots forming at the bottom surface of the films processed on 1.1 mm thick ITO substrate. However, this phenomenon cannot be observed in the films deposited on 1.8 mm thick FTO-based substrates with the normal fabrication conditions. We also found that the white dots will be formed even on the films fabricated with FTO substrate, if we drip the antisolvent preheated up to 45 °C. We therefore believe that the formation of the white dots is related to the cation exchange processes during the crystal growth (see the details in the main text). The cation exchange is a dynamic process, which is closely linked to the time dependence of the wet process. In the case of FTO, if the films were deposited with the hot antisolvent, the wet films tend to dry much faster than the case with the cold antisolvent. In the hot antisolvent dripping case, therefore, the whole cation exchange processes cannot be completed in time, resulting in white dots at the bottom surface of the films. In the ITO case, we may alleviate it by reducing the amount of GlyHCl added into the precursor solution and/or optimizing the fabrication conditions by, for example, i) changing the temperature of the antisolvent, ii) controlling the temperature inside the glovebox, or iii) dripping the antisolvent in a time window that ensures a sufficient time to complete the cation exchange within the whole crystallization process.

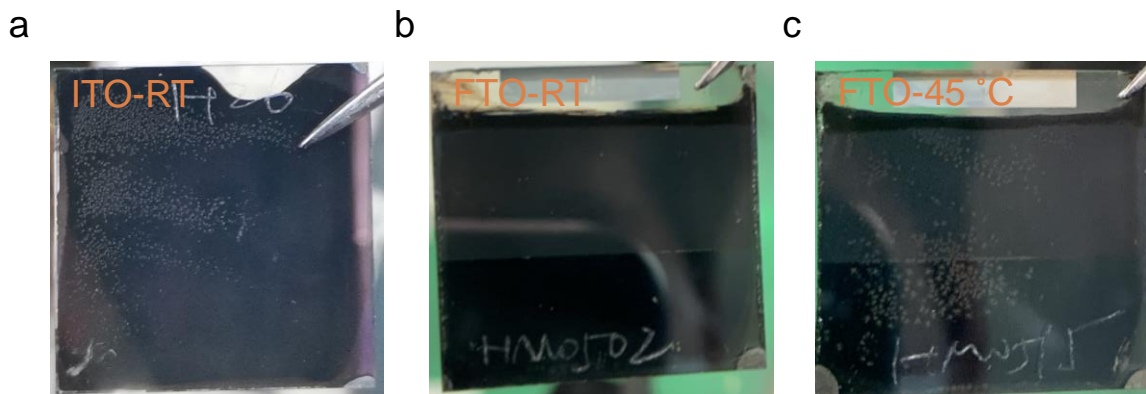


Fig. S47. The picture of the perovskite films fabricated with the addition of 2 mol% GlyHCl. **a**, The film deposited on ITO and **b**, FTO with the unheated antisolvent, **c**, the film deposited on the FTO with the antisolvent heated up to 45 °C.

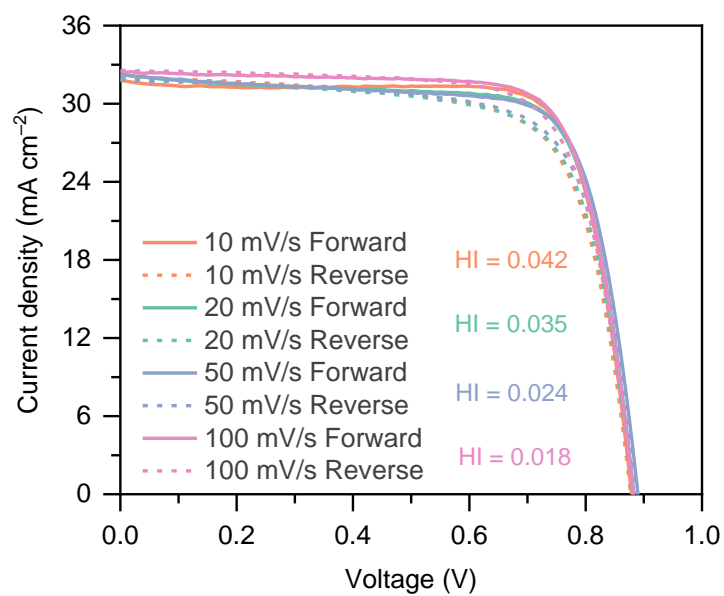


Fig. S48. J - V curves measured with scan speeds of 10, 20, 50, and 100 mV s⁻¹. The corresponding hysteresis index (HI) is 0.042, 0.035, 0.024, and 0.018, respectively. (HI = (PCE_{Forward} - PCE_{Reverse})/(PCE_{Forward} + PCE_{Reverse}))

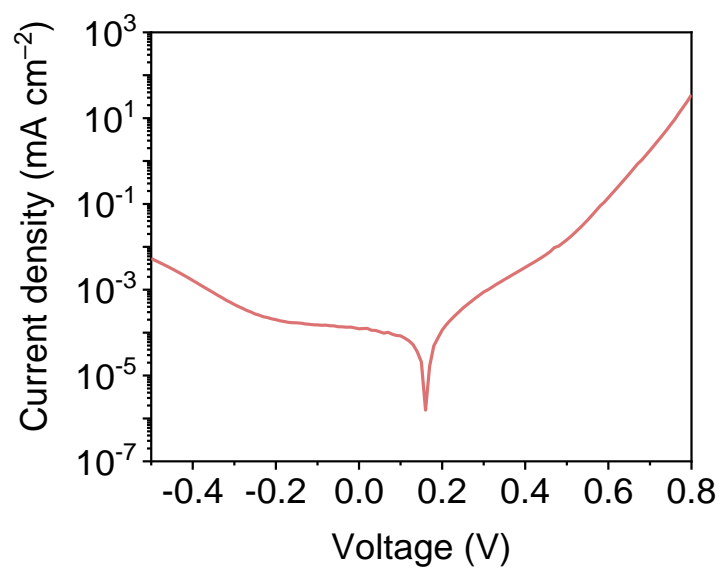


Fig. S49. Dark J - V curve of one representative EDAI₂/GlyHCl-treated device.

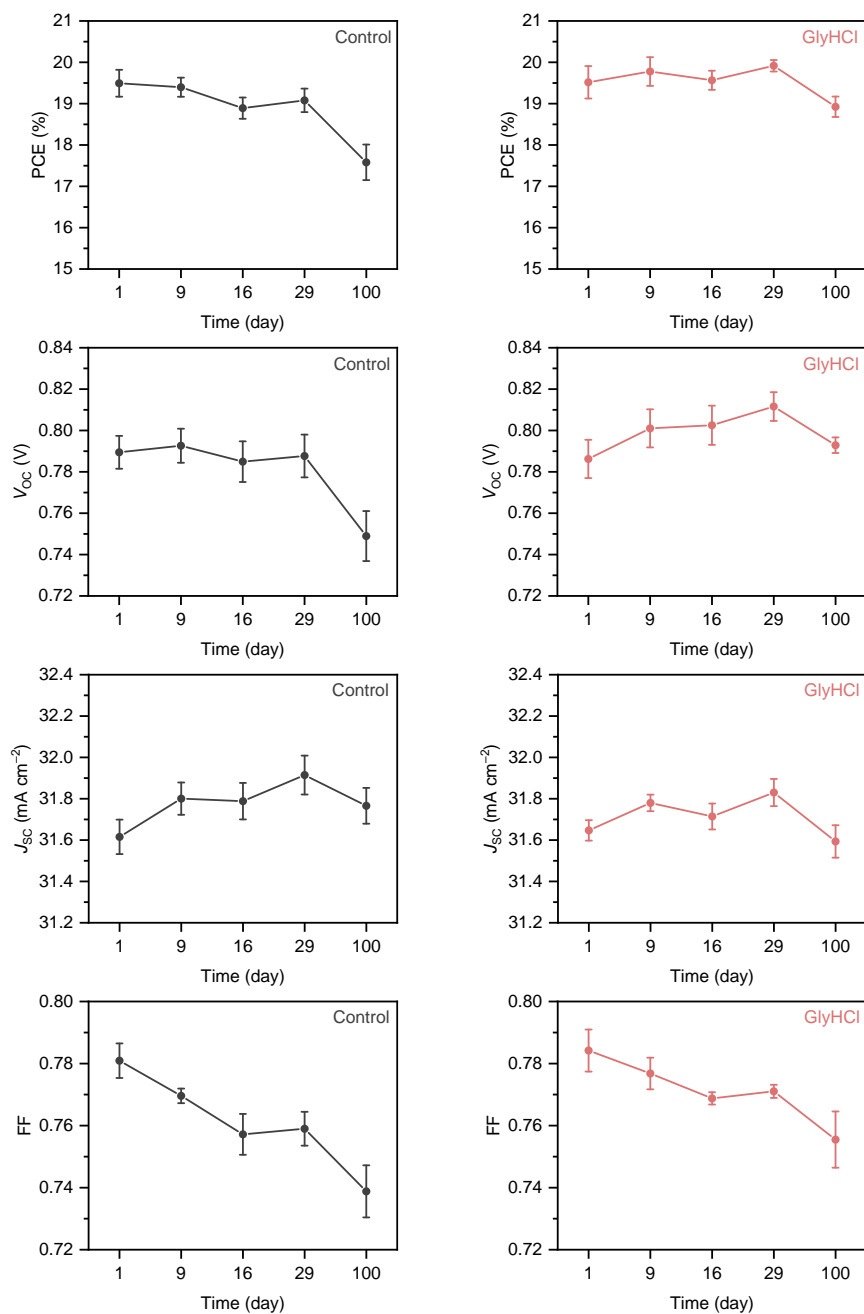


Fig. S50. Shelf-stability of the control and GlyHCl-treated devices stored in the dark in a N_2 -filled glovebox. The device parameters are calculated from the average measurements obtained from six cells of each type. After 100 days (2400 h) dark storage in the glovebox, the control device and device treated with GlyHCl additive retained 89 and 97% of their initial efficiencies, respectively.

Impedance characterization

The complex impedance data provides an accurate and detailed picture of the equivalent circuit resistances^{9,10}. Representative complex impedance scans for solar cell devices fabricated with the control, EDAl₂-treated, and EDAl₂/GlyHCl-treated perovskite layers are shown in Fig. S51a. The series resistance is minimal, while the parallel resistance, indicated by the diameter of the main semicircular feature, increases from 290 Ω cm² for the control film, to 445 Ω cm² for the EDAl₂-treated and 495 Ω cm² for the EDAl₂/GlyHCl-treated film. Under the measurement conditions, the parallel resistance (r_p) can be interpreted as the shunt resistance of the perovskite layer, and the higher values of the EDAl₂-treated and EDAl₂/GlyHCl-treated layers reflect the lower leakage current anticipated from the observed improvement in crystallinity and lower trap densities indicated by the SCLC measurements. The parallel resistance for the three devices values measured over a range of applied bias voltages are compiled in Fig. S51b. The overall trends observed in Fig. S51a are reproduced at all bias voltages below 0.3 V, while as the forward bias increases the resistance values decrease as the recombination currents increase.

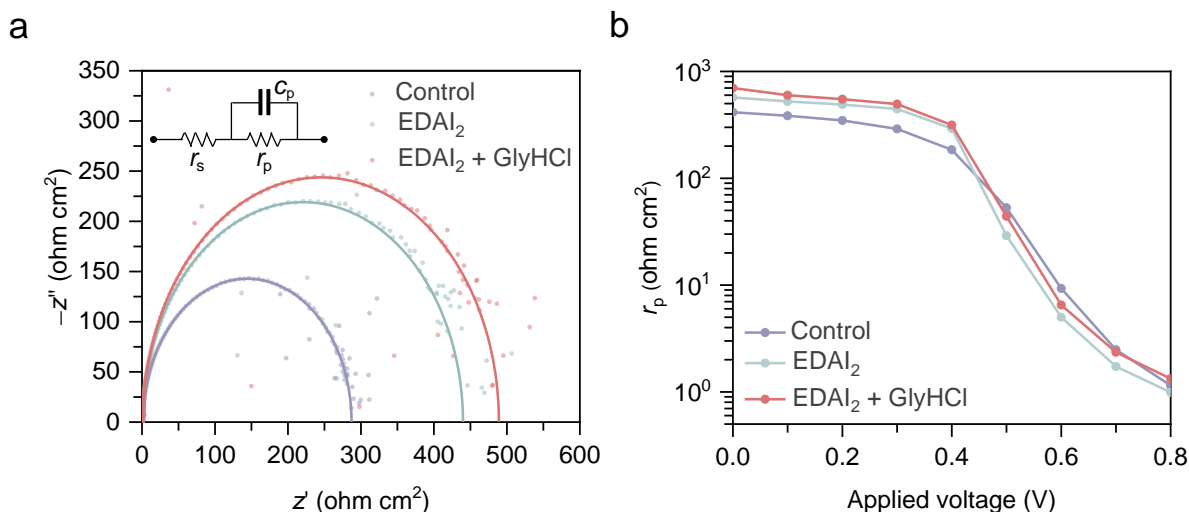


Fig. S51. a, Complex impedance of PSCs scanned over 20 Hz – 20 MHz, recorded at 0.3 V bias under AM1.5G illumination. **b**, Variations of parallel resistance in log scale as a function of applied voltage.

PLQY characterization

We fabricated perovskite films on PEDOT:PSS to evaluate the nonradiative recombination in our system via PLQY measurement. On PEDOT:PSS, the PLQY of the EDA_{I_2} /GlyHCl-treated perovskite film is 2.1%, considerably higher than that of the control film ($\sim 0.001\%$), verifying that the nonradiative recombination pathways in the EDA_{I_2} /GlyHCl-treated films are largely suppressed.

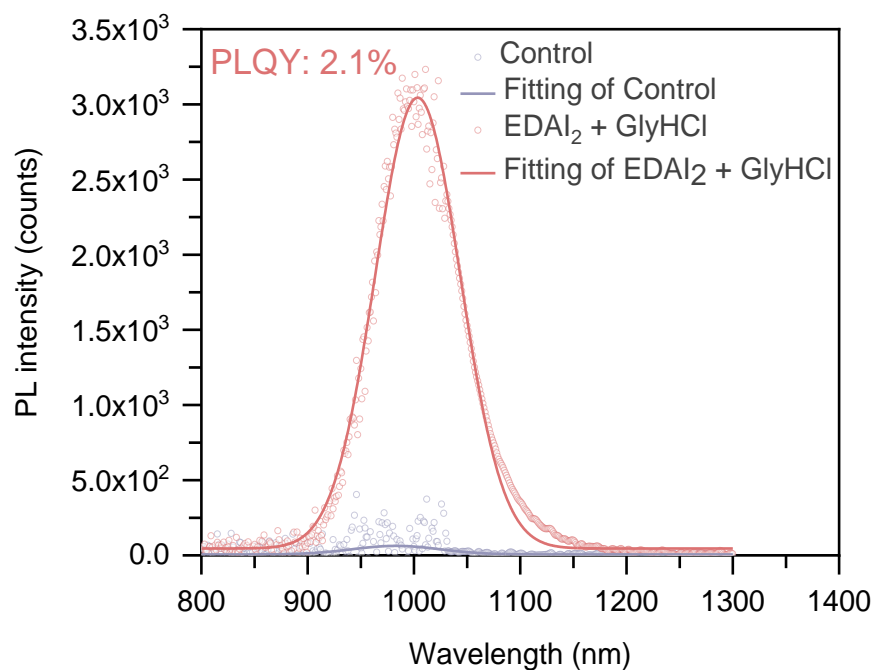


Fig. S52. PLQY spectra of the control and EDA_{I_2} /GlyHCl-treated perovskite films excited at 650 nm.

REFERENCES AND NOTES:

1. Yamada, Y., Nakamura, T., Endo, M., Wakamiya, A., and Kanemitsu, Y. (2014). Photocarrier recombination dynamics in perovskite $\text{CH}_3\text{NH}_3\text{PbI}_3$ for solar cell applications. *J. Am. Chem. Soc.* *136*, 11610–11613. 10.1021/ja506624n.
2. Tan, S., Huang, T., Yavuz, I., Wang, R., Weber, M.H., Zhao, Y., Abdelsamie, M., Liao, M.E., Wang, H.-C., Huynh, K., et al. (2021). Surface reconstruction of halide perovskites during post-treatment. *J. Am. Chem. Soc.* *143*, 6781–6786. 10.1021/jacs.1c00757.
3. Shahbazi, S., Li, M.-Y., Fathi, A., and Diao, E.W.-G. (2020). Realizing a cosolvent system for stable tin-based perovskite solar cells using a two-step deposition approach. *ACS Energy Lett.* *5*, 2508–2511. 10.1021/acsenerylett.0c01190.
4. Liu, D., Luo, D., Iqbal, A.N., Orr, K.W.P., Doherty, T.A.S., Lu, Z.-H., Stranks, S.D., and Zhang, W. (2021). Strain analysis and engineering in halide perovskite photovoltaics. *Nat. Mater.* *20*, 1337–1346. 10.1038/s41563-021-01097-x.
5. Yang, D., Zhou, X., Yang, R., Yang, Z., Yu, W., Wang, X., Li, C., Liu, S., and Chang, R.P.H. (2016). Surface optimization to eliminate hysteresis for record efficiency planar perovskite solar cells. *Energy Environ. Sci.* *9*, 3071–3078. 10.1039/C6EE02139E.
6. Zhang, Y., Wang, P., Tang, M.-C., Barrit, D., Ke, W., Liu, J., Luo, T., Liu, Y., Niu, T., Smilgies, D.-M., et al. (2019). Dynamical transformation of two-dimensional perovskites with alternating cations in the interlayer space for high-performance photovoltaics. *J. Am. Chem. Soc.* *141*, 2684–2694. 10.1021/jacs.8b13104.
7. Dong, Q., Fang, Y., Shao, Y., Mulligan, P., Qiu, J., Cao, L., and Huang, J. (2015). Electron-hole diffusion lengths $>175 \mu\text{m}$ in solution-grown $\text{CH}_3\text{NH}_3\text{PbI}_3$ single crystals. *Science* *347*, 967. 10.1126/science.aaa5760.
8. Shockley, W., and Queisser, H.J. (1961). Detailed balance limit of efficiency of p–n junction solar cells. *J. Appl. Phys.* *32*, 510–519. 10.1063/1.1736034.
9. Zarazúa, I., Sidhik, S., López-Luke, T., Esparza, D., De la Rosa, E., Reyes-Gomez, J., Mora-Seró, I., and Garcia-Belmonte, G. (2017). Operating mechanisms of mesoscopic perovskite solar cells through impedance spectroscopy and J – V modeling. *J. Phys. Chem. Lett.* *8*, 6073–6079. 10.1021/acs.jpcclett.7b02848.
10. Zarazua, I., Han, G., Boix, P.P., Mhaisalkar, S., Fabregat-Santiago, F., Mora-Seró, I., Bisquert, J., and Garcia-Belmonte, G. (2016). Surface recombination and collection efficiency in perovskite solar cells from impedance analysis. *J. Phys. Chem. Lett.* *7*, 5105–5113. 10.1021/acs.jpcclett.6b02193.